Stony Brook University

Defects Analysis of Wide Bandgap Semiconductor Single Crystals via Synchrotron White Beam X-ray Topography

A Thesis Presented

by

Shun Sun

to

The Graduate School

in Partial Fulfillment of the

Requirements

for the Degree of

Master of Science

in

Materials Science and Engineering

Stony Brook University

August 2013

Stony Brook University

The Graduate School

Shun Sun

We, the thesis committee for the above candidate for the

Master of Science degree, hereby recommend

acceptance of this thesis.

Michael Dudley – Thesis Advisor
Professor, Chair, Department of Materials Science and Engineering

Balaji Raghothamachar – Second Reader
Research Assistant Professor, Department of Materials Science and Engineering

T. A. Venkatesh – Third Reader
Assistant Professor, Department of Materials Science and Engineering

This thesis is accepted by the Graduate School

Charles Taber
Interim Dean of the Graduate School

Abstract of the Thesis

Defects Analysis of Wide Bandgap Semiconductor Single Crystals via Synchrotron White Beam X-ray Topography

by

Shun Sun

Master of Science

in

Materials Science and Engineering

Stony Brook University

2013

While the mature and well-established silicon technology, though after a long marvelous progress, exhibits some critical limitations with respect to its switching frequency, operation temperature, high power reliability and efficiency, a new generation of semiconductors, commonly referred to as "wide bandgap semiconductors", has emerged as promising candidate substrate materials that bear the capabilities to overcome those performance limitations. The inherent superior properties of those novel materials help broaden the extensions of semiconductor devices applications beyond those have been made from conventional materials like silicon, indium phosphide, and gallium arsenide. Potential revolutionary improvements coming into the cost, size, weight and performance of numerous incredible applications in both military and commercial field have already occurred and could be foreseen continued in the near future by the development of wide bandgap semiconductors.

As two important representatives in the class of wide bandgap semiconductors, silicon carbide (SiC) and aluminum nitride (AlN) are mainly studied in this thesis. New electronic devices based on SiC have demonstrated outstanding performance under extreme conditions such as high power, high temperature and high frequency. Due to the material's remarkable properties like high breakdown field, high efficiency power switching capability and high temperature reliability, no doubt it has huge potentiality in the applications of microelectronic systems. Besides the rather

higher bandgap that also makes it ideal candidate for the substrates in high power electronic devices, AlN's unique property--its wide direct transition energy range in ultraviolet has benefits in the realization of ultraviolet opto-electronic devices.

Though they have lots of advantages, the widespread commercial availability of these two materials remains retarded by the availability of large size commercial single crystal wafers of high quality at affordable price. Either for SiC or AlN, bulk crystal growth is no easy issue, for they cannot be manufactured in volume via the common liquid methods as utilized for Si wafer produce, due to the extreme conditions needed to melt them. Both of them are primarily grown in a unique way where vapor phase is involved, namely physical vapor transport (PVT) growth technique.

Since devices based on substrates with fewer defects have been demonstrated to have better performance, it is of great importance to obtain highly effective characterization techniques in order to get a better understanding of defect behavior. By analyzing the generation as well as the propagation mechanism, optimized growth strategies might be provided to help reduce or even eliminate those defects. The major techniques introduced in this thesis is synchrotron white beam X-ray topography (SWBXT) and it is in comparison with another frequently used technique—chemical etching. Nomarski optical microscope is also used complimentarily.

Two main topics covered in the thesis are:

1）Measurements of BPD densities in 4-inch 4H-SiC commercial wafers assessed using both KOH etching and topography methods are compared. The ratio of the BPD density calculated from topographic images to that from etch pits is estimated to be larger than $1/\sin\theta$, where θ is the offcut angle of the wafer. Based on the orientations of the defects in the wafers, a theoretical model is proposed to explain this disparity and two main sources of errors in assessing the BPD density using chemical etching are discussed.

2）The defect categories and distributions have been studied for six AlN single crystal wafers grown by sublimation recondensation technique. Transmission geometry in SWBXT of 3×{11-20}&3×{1-100}six reflections are carried out to map defects. Grazing-incidence reflection topography has also been taken for some selected areas for detailed analysis. Nomarski optical microscopy is used to supplement topography.

Table of Contents

List of Figures

Figure # **Page**

List of Tables

List of Abbreviations

BPD	basal plane dislocation
DIC	differential inference contrast
LAGB	low angle grain boundary
MP	micropipe
PVT	physical vapor transport
SEM	scanning electron microscope
SWBXT	synchrotron white beam x-ray topography
TED	threading edge dislocation
TEM	transmission electron microscope
TSD	threading screw dislocation
XRT	x-ray topography

Acknowledgments

First of all, I would like to express my deepest and sincerest appreciation to my advisor, Prof. Michael Dudley, for his generous and continuous support through my graduate education. His patience to the students, enthusiasms on the research topic and immense knowledge in the related science field have been of great value for me.

Second, my heartfelt appreciation goes to Dr. Balaji Raghothamachar for his instructive supervision on both the experiment operation and the thesis writing. Without his guidance, this thesis could not have been materialized.

Third, I would like to thank Prof. T.A. Venkatesh for kindly being my committee member and giving me valuable advices. His excellent teaching skill and broad and profound knowledge benefit me a lot in his core course *Strength of Materials*.

I also owe great gratitude to my lab colleagues in Synchrotron X-ray Topography Laboratory at Stony Brook University for not only their kind-hearted assistance during my research but also all the laughter we have had when working together during the last few years. Many thanks are given to Mr. Fangzhen Wu, Ms. Huanhuan Wang, Mr. Shayan Byrappa, Ms Hao Wang, Mr. Goue Ouloide, Mr. Jianqiu Guo, Ms. Yu Yang, and Mr. Tianyi Zhou.

Last but definitely not the least, I would like to express my special thanks to my family: my father Haitao Sun and my mother Qingying Yang. They are the most significant ones in this world for me and their unconditional spiritual support is the great power source in my life.

This work is financially supported in part by Dow Corning Corporation and from DARPA via Hexatech Inc. SWBXT work was carried out at the Stony Brook Synchrotron Topography Facility, Beamline X-19C, at the National Synchrotron Light Source (NSLS), Brookhaven National Laboratory (BNL), which is supported by the U. S. Department of Energy under Grant No. DE-AC02-76CH00016.

1 INTRODUCTION

It is widely known that the electronic revolution of the last century is attributed to the boom of the semiconductor industry and the whole power electronics world is built on the mature and well established silicon technology. Extended applications in automotive electronics, aerospace systems, communication engineering, and deep well drilling have been benefited from power devices made of semiconductors. However, with the rapid development of this field, the industry has been approaching a turning point where the theoretical limits of devices based on conventional semiconductor materials has been reached [1] and the new generation of semiconductor materials with higher ability to operate beyond the limitations are needed.

Wide bandgap semiconductors, as the name indicates, are semiconductors that have bandgap energies substantially exceed those of the prevailing semiconductor materials generally used before, such as silicon (Si), indium phosphide (InP), and gallium arsenide (GaAs). No specific criterion has been set to define how wide could be termed wide though, any semiconductor material with a bandgap energy larger than 2 eV falls into this category [2]. Their broad gaps in terms of electronic band energy provide those materials incomparable advantages and make them ideal candidates for the products operating in extreme conditions such as high power, high frequency and high temperature environment [3-8]. Take the operation temperature as an example. Literatures indicate that standard commercial Si-based devices could function properly in the temperature no more than 125 °C [9, 10], and operating at ambient temperatures beyond 150 °C would be problematic [10]. As a contrast, devices made based on silicon carbide (SiC)—one of the dominantly studied and used wide bandgap materials, are reported to operate at a working temperature up to 600 °C [11-14].

Except for diamond, most wide bandgap semiconductors that have attracted researchers' attentions are compound materials such as SiC, gallium phosphide (GaP), gallium nitride (GaN), zinc oxide (ZnO), and aluminum nitride (AlN). The family of $A^{III}B^{V}$ type of compounds occupies a significant part among them. Though the inherent outstanding properties of those materials have provided promising possibilities for them to become the crucial semiconductors for the next generation, the realization of their widespread commercial applications has been staggered by the availability of large amount bulk materials of high quality at a reasonable cost. Accordingly, numeous studies have been carried out on both the crystal growth methods and the defects characterization techniques of those materials. In terms of this writing, focus has been cast on two major materials

that bear bright potentiality in continued revolutionary improvements for a variety of microelectronic and optoelectronic applications in terms of efficiency, size, cost, and reliability [12, 15-17]. After a brief introduction to the background knowledge of the material properties as well as the popular crystal growth techniques of those two materials, detailed discussion will be carried out on the characterization methods used in this study for revealing the internal imperfections of semiconductor single crystal substrates. At the end, deep analyses of a variety of defects observed in the two materials are reported.

1.1 Structure, Properties, and Applications of Materials

1.1.1 Structure, Properties, and Applications of SiC

Ever since Cree Inc. released the first commercially available SiC wafer in 1991, the past two decades has witnessed the amazingly rapid progress in the development of high quality SiC single crystal growth and its employment in novel and innovative power electronic devices. It has already developed into the most mature one among all band gap semiconductors. Wafers with larger and larger diameter, but lower and lower density of defects are emerging in an endless stream. Thanks to the efforts made by worldwide researchers and manufacturers, the common size of SiC wafers in the market up to date has increased to 4-inch and 6-inch wafer is at hand. Meanwhile the SiC-based device fabrication technique is also steadily stepping forward and the boost in the size has helped driven down the average device cost remarkably.

From a crystallographic point of view, SiC is mostly notable for its amazingly large number of polytypes. In total, more than 200 polytypes have been discovered in SiC and most of them are hexagonal or rhombohedral structures, except for 3C-SiC (also known as β-SiC), which is the only cubic type with the zincblende structure. Each type of SiC is composed of tetrahedrons that consist of four silicon (carbon) atoms at their corners and a carbon (silicon) atom at the centroid. In the tetrahedron, any of the four Si-C bonds could be considered as a c-axis with a triangular base that is normal and opposite to this c-axis, defined as a c-plane, also known as the basal plane. Each c-axis also represents a direction about which the tetrahedron has threefold symmetry, meaning that once a rotation of 180° is taken along the c-axis, the trigonal symmetry would be broken and a "twinned" variant tetrahedron is produced. As a matter of fact, different SiC polytypes are merely different assemblies of normal and twinned tetrahedrons along the c-axis [18-20]. Fig.1-1 shows the twin variants of tetrahedrons in the SiC crystal structure.

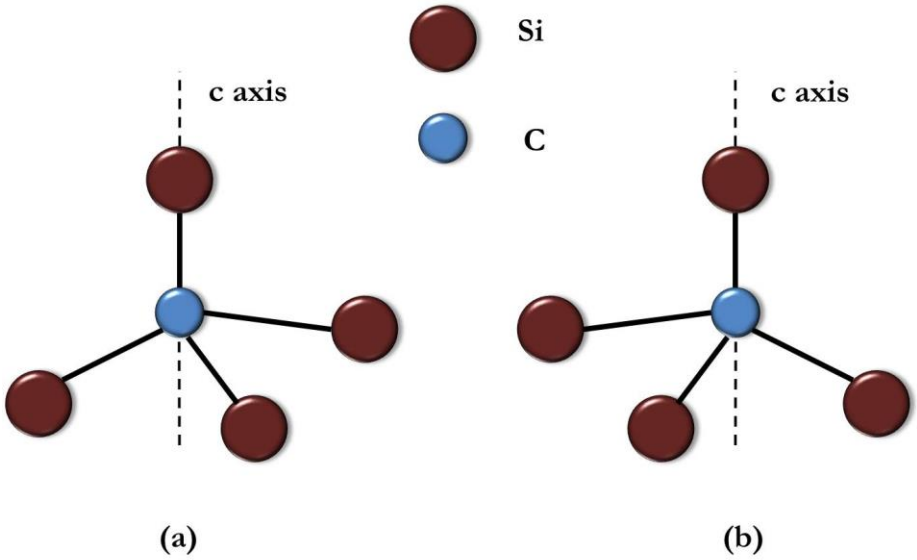

Figure 1-1 (a) SiC tetrahedron with the c-axis coinciding with the vertical Si-C bond; (b) the twinned variant of the SiC tetrahedron. The two variants are related to each other by a 180°rotation around the c-axis.

Among all the different SiC polytypes, *3C*-SiC, *4H*-SiC, and *6H*-SiC are the most popular ones. Though *3C*-SiC is often observed, there is no mature method for its large-size and high-quality growth and therefore it is not discussed further here. The other two polytypes are the far superior forms of semiconductor device quality SiC commercially available in mass-produced wafer form [21]. Figure 1-2 shows the projection of the structures of *4H*-SiC and *6H*-SiC onto the (11-20) plane. As could be seen from the image, *4H*-SiC and *6H*-SiC have four and six Si-C bilayers, respectively, in their corresponding hexagonal unit cell with the stacking sequences "ABACABAC…" for *4H*-SiC and "ABCACBABCACB…." for *6H*-SiC.

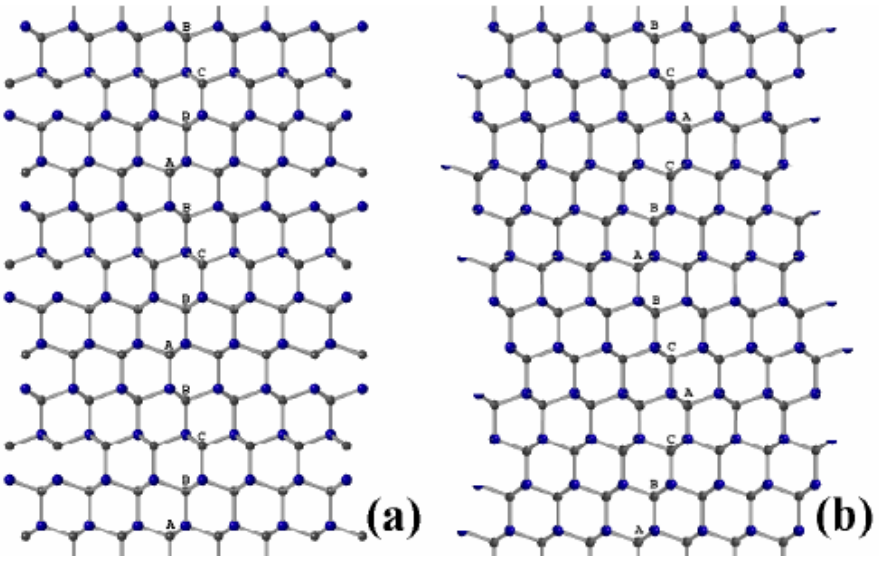

Figure 1-2 Projection of *4H*-SiC (a) and *6H*-SiC (b) structure into (11-20) plane. Small and large balls indicate C and Si atoms, respectively. The stacking sequence for *4H*-SiC is "ABCB…" and "ABCACB…" for *6H*-SiC. (Provided courtesy by Yi Chen [111].)

All the SiC polytypes are semiconductors possessing favorable electronic properties such as higher electron mobility, larger breakdown field, higher thermal conductivity compared with other traditional semiconductor materials. It should also be pointed out that being the only compound semiconductor that has the native oxide SiO_2 gives SiC the greatest advantage over other conventional semiconductor materials [22]. The comparison of some selected important semiconductor electronic properties of major SiC polytypes with Si, GaAs, and 2H-GaN at the temperature of 300K is given in Table 1-1[23-31]. In the table it is clear to see that compared to Si, which is used as the evaluation standard for comparison, SiC has a thermal conductivity at least twice higher and a breakdown field nearly five times higher. The saturated carrier velocity of SiC is also twice that of the Si.

Table 1-1 Comparison of Selected Important Semiconductor Electronic Properties of Major SiC Polytypes with Silicon, GaAs, and 2H-GaN at 300K

Property	Si	GaAs	4H-SiC	6H-SiC	2H-GaN
E_g (eV)	1.1	1.42	3.2	3.0	3.4
Relative dielectric constant	11.9	13.1	9.7	9.7	9.5
E_b (MV/cm) $N_D = 10^{17}$ cm-3	0.6	0.6	//c-axis: 3.0 ⊥c-axis: 2.5	//c-axis: 3.2 ⊥c-axis: >1	2-3
k (W/cm·K)	1.5	0.5	3-5	3-5	1.3
Intrinsic carrier concentration (cm^{-3})	10^{10}	1.8×10^{6}	$\sim10^{-7}$	$\sim10^{-5}$	$\sim10^{-10}$
μ_e ($cm^2/V\cdot S$)	1200	6500	//c-axis: 800 ⊥c-axis: 800	//c-axis:60 ⊥c-axis:400	900
μ_h ($cm^2/V\cdot S$) $N_A = 10^{16}$ cm^{-3}	420	320	115	90	200
V_s (10^7 cm/s)	1.0	1.2	2	2	2.5

E_g: band gap; E_b: breakdown field; k: thermal conductivity; μ_e: electron mobility; μ_h: hole mobility; V_s: saturated carrier velocity. (Source: data compiled from references [23-31].

The major applications of SiC in electronic devices involve high-temperature devices, high power devices and high frequency devices. The intrinsic carrier concentration is a key factor in choosing the proper semiconductor material for device fabrication because semiconductor electronic devices function properly only in the temperature range where intrinsic carriers are negligible so that introduced dopant impurities domainate the conductivity [26]. As for high temperature devices, the intrinsic effects of SiC do not occur until very high temperature [6], and this feature leads to important benefits to applications in automotive sensors, aviation sensors, spacecraft sensors and controls and deep-well drilling industries [6, 32-35]. The high breakdown field of SiC leads to a thinner as well as heavier doped blocking voltage region of the power device. Efficiency of the device is increased by the high reverse blocking voltage with lower series resistance. The applications of SiC in high power devices include switching devices such as MOSFETs, high-power rectifiers, high-power switching transistors, etc. For high frequency devices, SiC-based high-frequency RF MESFETs for cellar base stations are now commercially available [36].

Another important application (also the earliest application) of SiC material is in the optoelectronic devices. In 1989, Cree Research Inc. introduced the first 6H-SiC-based pn junction light-emitting diodes (LEDs) as the first semiconductor devices to cover the blue portion of the

visible color spectrum [37]. Even though LEDs based on SiC pn junctions are inefficient due to the indirect bandgap of SiC and are gradually replaced by much more efficient direct-bandgap GaN and other III-Nitrides blue LEDs, SiC wafers are still employed as the substrates for devices made with Group III-Nitrides [38].

1.1.2 AlN's Structure, Properties and Applications

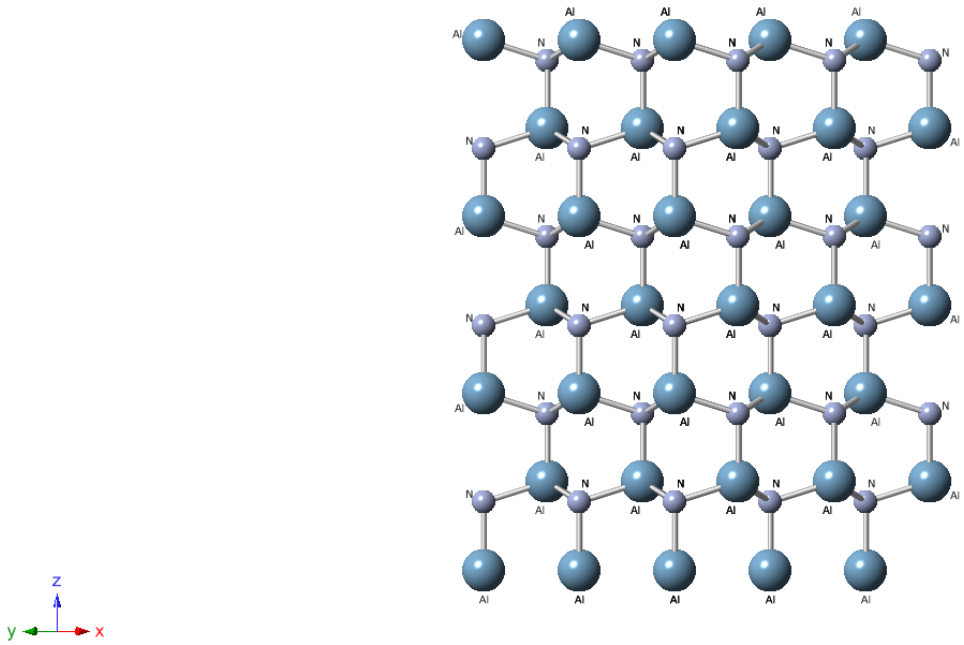

Figure 1-3 Projection of AlN structure into (11-20) plane.

Aluminum nitride in wurtzite phase (w-AlN), belonging to the $P6_3mc$ space group, has the similar crystal structure with α-SiC, being a tetrahedrally coordinated compound with in-plane hexagonal lattice constants a=3.110 Å and c=4.980 Å [39]. Though the 2H wurtzite structure is the most common polytype seen among the AlN grown naturally, crystals in cubic zincblende structure have also been artificially made out successfully under certain lab conditions [15]. Notwithstanding the wurtzite structure indicates the presence of covalent bonds, X-ray diffraction experiments have revealed that a significant ionic component contributes to the bonding in AlN, due to the almost two times disparity between the electronegativities of the aluminum atoms and the nitrogen atoms: 1.6 and 3.0, respectively [40]. Fig. 1-3 is a projection of AlN structure into (11-20) plane.

The superior optical and high-temperature electronic properties of AlN, attributed to its high transparency of ultraviolet light, relatively large direct bandgap energy (~6.2 eV at 300K) [41] and high thermal conductivity, makes it one of the most promising III-V semiconductors for short-wavelength opto-electronic devices and for high-frequency and high power electronics. Table 1-2 displays some selected important properties of AlN in wurtzite phase. Table 1-2 shows some important properties of AlN in wurtzite phase. At T=300K, the band gap energy of AlN single crystal is about 6.2eV, much larger compared to that of other III-V compound semiconductors, like InN (~1.9eV) or GaN (~3.4eV) [15].

Table 1-2 Selected Major Properties of Wurtzite AlN. (Souce data compiled from Ref. [42]-[50].)

Band gap Energy	E_g (300K) = 6.2eV E_g (5K) = 6.28eV
Coefficient of thermal expansion	$\frac{\Delta a}{a} = 4.2 \times 10^{-6}/K$ $\frac{\Delta c}{c} = 5.3 \times 10^{-6}/K$
Thermal conductivity	$\kappa = 2\ \mathrm{W/cm}K$
Dielectric constants	$\epsilon_0 = 8.5 \pm 0.2$ $\epsilon_\infty(E \perp c) = 4.68$
Electron mobility	$1100\ cm^2/Vs$

The high thermal conductivity, as its most distinguished property, together with the low coefficient of thermal expansion, high electrical resistivity, and moderate dielectric loss provides AlN remarkable advantages in its potential applications as substrates for microelectronics packages [51]. The majority state-of-art high electron mobility transistors (HEMTs) were fabricated on AlInN/AlN/GaN heterostructures grown on SiC substrates [52-54]. Used for highly efficient power conversion, they are strongly promising in the future for the high-frequency and high power operation in hybrid vehicles and green-energy systems.

Due to its wide direct transition energy range in ultraviolet, AlN has long been considered as a powerful candidate material for the realization of deep ultraviolet laser diodes (UVLD) or ultraviolet light-emitting diodes (UV-LED). Those UV optoelectronic devices based on AlN substrates have the capability of generating light in the short-wave ultraviolet radiation (also called UV-C band) (200-280 nm), leading them to the great utilization in a considerable number of application fields including drinking water treatment, air purification, curing of varnishes and

polymers, and medical disinfection [55-60]. For example, when water is exposed to UV light, the UV-C light near 265 nm most effectively help break up the chemical bonds within DNA or RNA of the bacteria, viruses and spores in the water and thus they are prevented from replication and eventually end up inactive [61]. Compared to other III-nitride semiconductors, AlN substrate is the optimum choice for devices working at this wavelength.

1.2 Crystal Growth Methods of Major Wide Bandgap Materials

Ultrahigh-quality wide bandgap semiconductor single crystals are in great demand nowadays, while the difficulties in crystal growth remain challenging for their mass production. Unlike silicon or gallium arsenide, both SiC and AlN cannot be manufactured through the traditional Czochralski or Bridgeman methods that both involve bulk growth of crystals from liquid phase, for these two materials sublimate before they melt into liquid in an atmospheric environment. To grow them in traditional ways, extremely high temperatures and pressures are required and thus would increase the cost drastically. As for the bulk crystal growth of these materials, a vapor phase transport growth process is established.

First technique developed for SiC crystal growth occurred in 1955, and it was a sublimation method called Lely method, named after its creator [62]. In 1978, a modifided seeded sublimation growth process for SiC, later referred to as the seeded modified Lely process (also termed as physical vapor transport process), has been developed by Tairov and Tsvetkov [63, 64]. It has been marked as a breakthrough indicating that the new era of realization of producing large cross-section area single crystal boules of SiC was at hand. In the physical vapor transport (PVT) growth technique, a polycrystalline SiC (powder)source is placed in a semi-closed crucible, heated up to 2400 °C in an argon environment under the pressure of 1~750 Torr and it sublimes into the vapor phase [65]. A SiC single crystal of ultimate quality, namely the seed material, is placed at the other end of the funace. Due to the temperature gradient, the vapor spreads to the seed where lower temperature compared to that of the source material is maintained, and condenses there. Consequently the seed material grow bigger and bigger and a boule is obtained, further to be sliced into wafers and polished as required. Fig. 1-3 gives a simple skech-up (Fig. 1-4(a))of how a c-plane wafer is cut from the crystal boule grown along c-axis, i.e. <0001> direction and shows the corresponding crystallographic directions on the c-plane (Fig. 1-4(b)).Usually, the preferred growth direction in PVT growth process is [0001] crystallographic direction (c-axis), though crystal grown along other

directions, for example, a-axis, are also under investigation. Originally, the source material was placed in the upper part of the graphite cruible and the seed at the bottom [63-64, 66]. Using this arrangement, Ziegler et al. reported successfully growing 6H-SiC with a length of 24 mm and a diameter of 20 mm [66]. However, in the configuration that is commonly used today, the seed is held on the top while the source SiC is on the bottom, leading to a higher yield and gradualy becoming the industry standard[67, 68]. Fig. 1-5 is a schematic illustration showing the view of growth cell in this configuration. Up to date, using PVT technique to grow 4-in commercially available SiC single crystals is developed pretty maturely and larger wafers with diameter of 6-inch are also successfully realized by some vendors [36, 69-70].

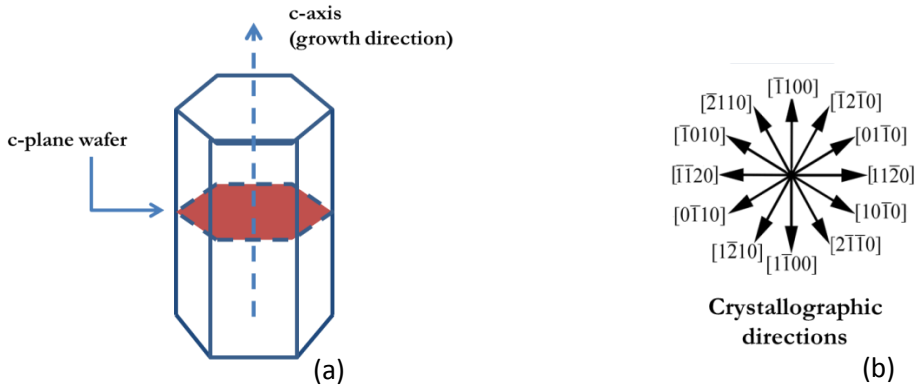

Figure 1-4 a) A sketch demonstrates how a c-plane wafer is cut from a crystal boule whose growth direction is c-axis <0001>; and b) an illustration of the crystallographic directions of the c-plane.

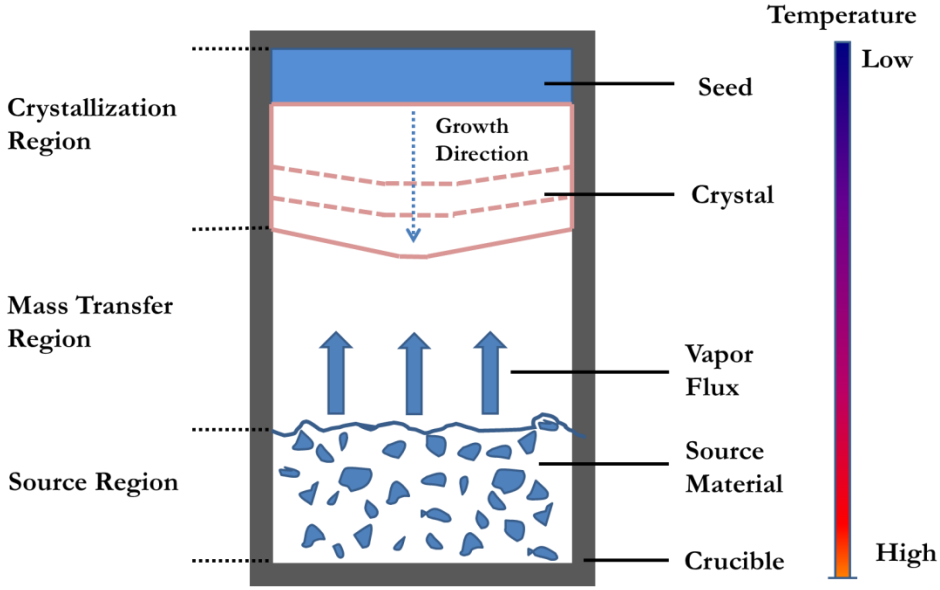

Figure 1-5 Schematic view of growth cell for SiC single crystals grown by PVT technique.

First reported by Slack and McNely [71, 72], PVT growth technique is also utilized in the growth process of AlN single crystals. In some literature it is also termed as sublimation-recondensation growth technique [73, 74]. During the growth process, the AlN powder is placed at the bottom of a reaction crucible, inside which the ultra-high purity nitrogen ambient is applied. The powder sublimes at the temperature above 2000 °C and under the pressure of 300~800 Torr, decomposes into nitrogen and aluminum gases, then transports through the vapor phase to the seed material located on the top of the crucible where lower temperature is kept. As soon as they condense on the surafce of the seed, the crystal starts to grow by recrystallization. The growth unit setup is similar to that in the SiC crystal growth. (See Fig. 1-5) The complete reactions during the process can be written as:

$$AlN_{(s)} \xrightarrow[T_{growth}+\Delta T]{sublimation} Al_{(g)} + \frac{1}{2}N_2 \xrightarrow[T_{growth}]{Deposition} AlN_{(s)}$$

AlN does not exist in nature and thus there is a lack of high quality AlN single crystal when it comes to the supply of seed materials. For a long time, foreign substrates such as Si, SiC and sapphire have been used as the seed for the bulk AlN single crystal growth. Nevertheless, critical issues have inevitably arose due to the lattice mismatch, the disparity in the thermal expansion coefficients, and the chemical incompatibility, causing negative impact on the generation of defects grown at the interface and further extended into the AlN layer. Hence, continuous efforts have been made on the investigations of growth of large AlN single crystal seeding on GaN substrates or self-seeding growth [75-78]. Besides the often c-(0001) orientation grown crystals, m-(10-10) orientation crystals of seeded growth of AlN boules by PVT technique has also been achieved [79].

The key issue in the PVT growth technique is to make sure the temperature gradient and gas pressure under control, for the quality of crystal would be seriously impacted otherwise. For SiC, undesired polytypes might come into formation when the growth temperature is offset since different polytype require different formation energy that related to the growth temperture. Woo Sik Yoo and Hiroyuki Matsunami from Kyoto University observed that as a single crystalline *3C*-SiC sample was heated at temperature from 1800 to 2400 ℃ in an Ar atmosphere, a solid-state phase transformation from *3C*-SiC to *6H*-SiC occurred above 2150 ℃ [80]. The reason an argon overpressure is maintained during the heating process is to avoid crystallization at lower temperature, minimizing the chance of which undesired polytype would occure. For AlN, though not bothered by the polytype issue, the generation of second grain, the accumulation of inclusions and other growth defects are also introduced by losing control of the growth conditions. Fig. 1-5 shows the hex

inclusions and secondary grains observed with a nomarski optical microscope from a PVT-grown AlN wafer.

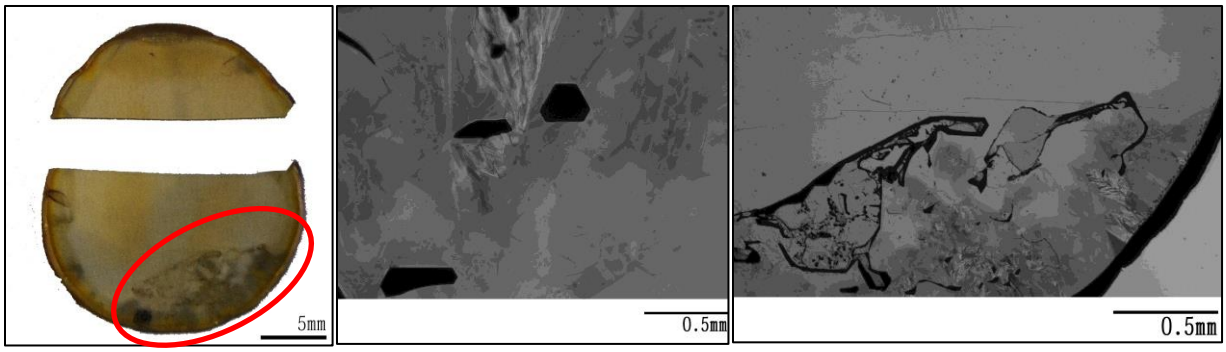

Figure 1-6 a) The optical image of a PVT-grown AlN wafer (broken into two parts). b) & c) Close look at the region that has been circled out in a) via Nomarski optical microscope shows the present of hex inclusions and second grains that might be caused by the poor control of the growth conditions.

1.3 Major Defects Observed in Current Materials

1.3.1 Major Defects Observed in SiC Substrates

The majority defects observed in the SiC substrates up to date could be classified into two categories: one is growth dislocations and the other is deformation induced dislocations. The former comes into formation during the growth and threads through the crystal with the moving growth front. Those dislocations, including threading edge dislocations (TEDs), threading screw dislocations (TSDs), and micropipes (MPs), could originate from the continuation of the dislocations previously present in the seed, or from the relaxation of stresses arising from: 1) handling damage on the surface of the seed; 2) the incorporation of inclusions of solvent or impurity that can occur on the seed surface or later during growth that can be equivalently viewed as imperfect lattice closure around such inclusions; and 3) coalescence between two or more misoriented growth centers [81]. As the name indicates, those threading dislocations all have line directions roughly aligned along with the growth direction [0001]. While TEDs have Burgers vector **b**=1/3<11-20>, which is perpendicular to their line direction, both TSDs and MPs have Burgers vector **b**=n<0001>, parallel with the line direction [0001]. The major difference between MPs and TSDs is the magnitude of the Burgers vector. As n gets larger, the close core threading screw dislocations become huge ones with open cores, namely micropipes.

The deformation induced dislocations can be induced either by mechanical stress or by electrical stress like electron-hole recombination. The perfect basal plane dislocations, as induced by

plastic deformation process and often glide under thermal shear stress, are the most widely observed type of dislocations in PVT-grown SiC crystal. They have line directions parallel with the basal plane (0001), with Burgers vector **b**=1/3<11-20>. Fig. 1-7 shows a schematic of those basic dislocations introduced above that commonly observed in SiC substrates.

Among four types of defects mostly commonly observed and studied in SiC substrates—MPs, TEDs, TSDs, and BPDs while significant progress has been made in decreasing the density of MPs [82], the latter three are attracting increasing attention since they are reported to result in detrimental influence on various SiC-based devices [83-85]. Especially for BPDs, a variety of studies have been done regarding the expansion of the Shockley stacking faults present at their cores that would introduce undesired forward voltage drift during device operation [86-88]. Previous literature has also reported on the conversion and multiplication of BPDs from substrates to epilayer [89, 90].

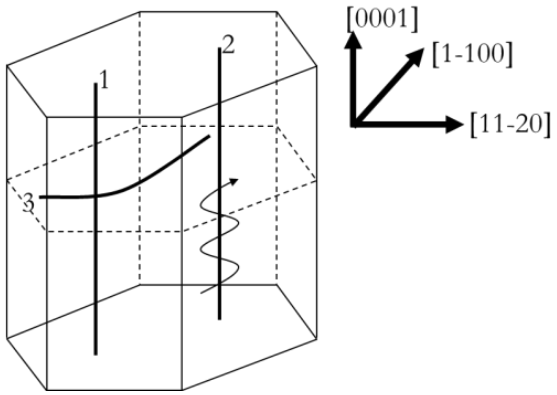

Figure 1-7 Schematic of the major defects observed in SiC substrate. 1—threading edge dislocation; 2—threading screw dislocation; 3—basal plane dislocation.

1.3.2 Major Defects Observed in AlN Substrates

Most defects having been detected in AlN substrates so far are similar to those in SiC samples. The majority of them are BPDs and threading dislocations. In some regions where the dislocation density is rather high, BPDs or threading dislocations, or sometimes both, aggregate together into small angle boundaries. Besides, another critical issue regarding the quality of the AlN substrates is the inclusion contamination. Further discussion will be conducted in the **Results & Discussions** part.

2 EXPERIMENTAL –CHARACTERIZATION METHODS

The high-pace developing semiconductor industry and its essential demand for nearly perfect semiconductor single crystals have given impetus to the improvement of the various characterization techniques in this field. As each technique has its own fundamental working principles, whether based on optical, electron, chemical reaction or X-ray diffraction, they all have their natural merits as well as limitations. The major technique introduced in this paper is a non-destructive characterization method called X-ray topography, and synchrotron white beam is used as its radiation source. Other two techniques—molten potassium hydroxide (KOH) and Nomarski Optical Microscopy are also utilized in a subsidiary way.

2.1 Synchrotron X-ray Topography

2.1.1 Introduction

The first experiment during which an X-ray topographic image was recorded was carried out by Berg. VW in 1931[91], when he used characteristic radiation incident at a very small angle to the surface of a single crystal and obtained a striated image where the point-to point variation of the reflected intensity revealed the plastic deformation inside the crystal. Though several studies on the X-ray topography technique have been taken out [92-95], it was not until 1958 when Lang developed a profound transmission technique that made imaging individual dislocations in the single crystal possible [96] did people realize the huge potentiality of this technique in the application of defects characterization of single crystal materials.

Ever since the advent of synchrotron radiation sources and its application into the field of X-ray topography brought by Tuomi [97], synchtrotron X-ray topography has been developed as a powerful tool to analyze various defects extended inside the entire volume of the large single crystals and sometimes even characterize the wafers with devices fabricated on them [81]. Compared to other widely used characterization techniques, like scanning electron microscopy (SEM) or transmission electron microscopy (TEM) from which only local information of a very tiny area of the sample could be provided at one time, X-ray topography is capable of giving the images of defect distribution throughout the sample during a very short range of operation time, with very simple, if not none, sample preparation. Compared to electrons, X-ray has stronger power in

penetrating and therefore the samples used for X-ray topography have larger tolerance in terms of thickness and shapes. They can vary from very thin foil to bulk materials. Besides, the outstanding properties of synchrotron radiation source, including the high brightness, tunability, and natural collimation, largely benefit the topography images in both spatial resolution and strain resolution [98]. The exposure time has also been reduced dramatically from several hours per cm^2 to seconds per cm^2 when synchrotron radiation has taken place of the conventional X-ray source.

Though both monochromatic and white source could be used in synchrotron X-ray topography, the latter one is chosen for our experiments. Similar to the Laue transmission technique, white radiation topography has superior capabilities that resulted from the high intensity of the synchrotron beam and the natural collimation. The latter leads to the possibility of using very long beamlines (~25m) to maximize the area of the beam falling on the sample. With this benefit, samples of relatively large scale could be examined rapidly. What's more, with the broad range of radiation spectrum in white beam topography, multiple images of different reflections could be obtained simultaneously (Fig.2-1), contributing to a great improvement in the rate of data acquisition.

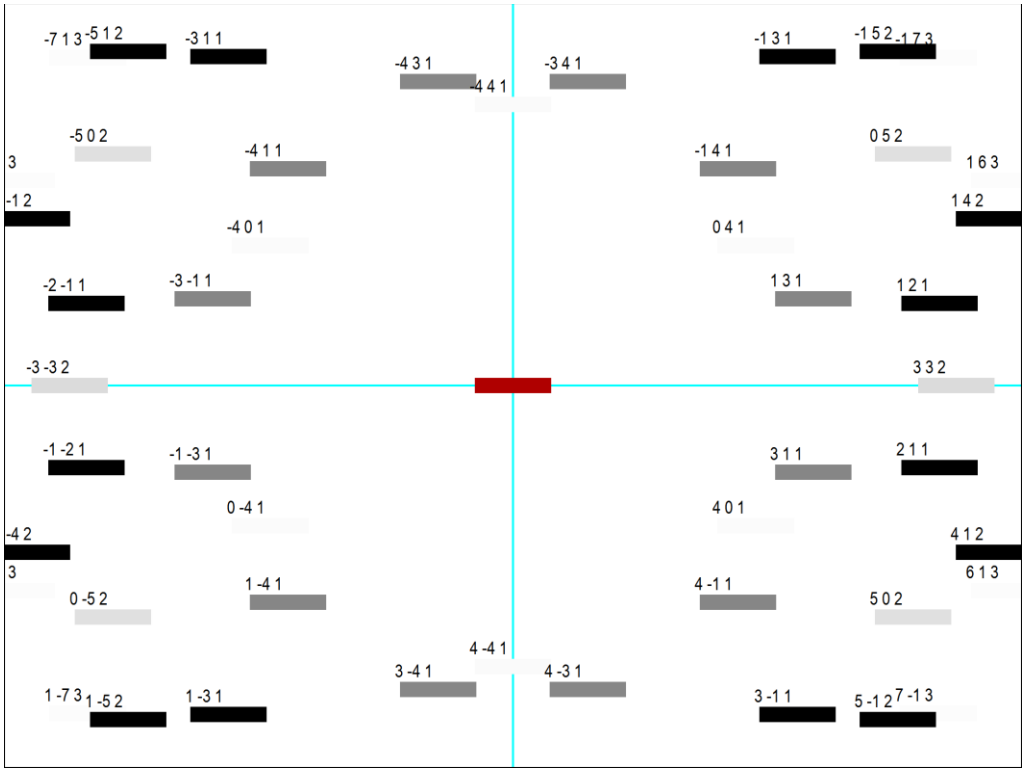

Figure 2-1 Computer simulation of indexed transmission Laue pattern of AlN with surface plane orientation (0001) and side plane (11-20). Sample to film distance is set as 20 cm. (The program used to generate the simulated pattern is LauePt., provided courtesy of Dr. Xianrong Huang.)

2.1.2 Experimental Arrangements

To understand the principle of the experiment settings, it's better to recall the Laue diffraction method that mainly used to determine the orientation and to evaluate the quality of a large single crystal. In the Laue method, the crystal is fixed and the white radiation transmits through or reflects from it (Fig. 2-3). According to the Bragg's Law, for diffractions to happen the following condition should be satisfied:

$$2d\sin\theta = n\lambda$$

where d is the plane spacing, λ is the wavelength of the incident beam and θ is the diffraction angle. n is an integer. Therefore in the Laue diffraction, where the diffraction angle is fixed and a bunch of radiation beams of different wavelengths are involved, different set of crystal planes inside the sample selects their own radiation of the wavelength that satisfies the diffraction condition and thus a diffraction pattern composed of multiple diffraction spots are obtained at one time. No magnification is involved in this process.

Three fundamental experimental arrangements are involved in Synchrotron White Beam X-ray Topography (SWBXT)—transmission, back-reflection, and grazing-incidence, as illustrated in Fig. 2-2. In the transmission mode (Fig. 2-2 (a)), the diffracted spots fall on the film with the direct beam passing through the sample that has been held on a sample holder between the radiation source and the film. The holder could be rotated around three axes. According to the diffraction pattern symmetry, the surface and side plane orientation of the sample is detected and then, by rotating the sample in certain ways, the desired diffraction spot is picked out. For large sample which cannot be covered in one shot due to the limitation of the beam size, a slit is placed between the film and the sample for image scanning, during which process the sample and the film move together. Transmission mode is often used for the study on BPDs, which usually appear as a dark single line or double lines in transmission images (See Fig. 2-3 (a)). In the back reflection mode (Fig. 2-2 (b)), the film is placed between the sample and the X-ray source. Large Bragg angles are involved in this mode (typically 80°), and it is advantageous in recording the threading screw dislocations that shows white circular contrast on the film (Fig. 2-3 (b)). In Fig. 2-3, a typical back reflection X-ray topography showing SDs and MPs is a typical transmission X-ray topography showing BPDs. The grazing-incidence reflection mode is usually used for the characterization of the features near the surface. In this mode, the sample is nearly parallel to the beam, with a slight incident angle (typically

2°) (See Fig. 2-2 (c)). Fig. 2-4 (a) & (b) are the photos taken at the NSLS X-19C beamline showing the experiment setups for a) transmission topography and b) grazing-incidence topography.

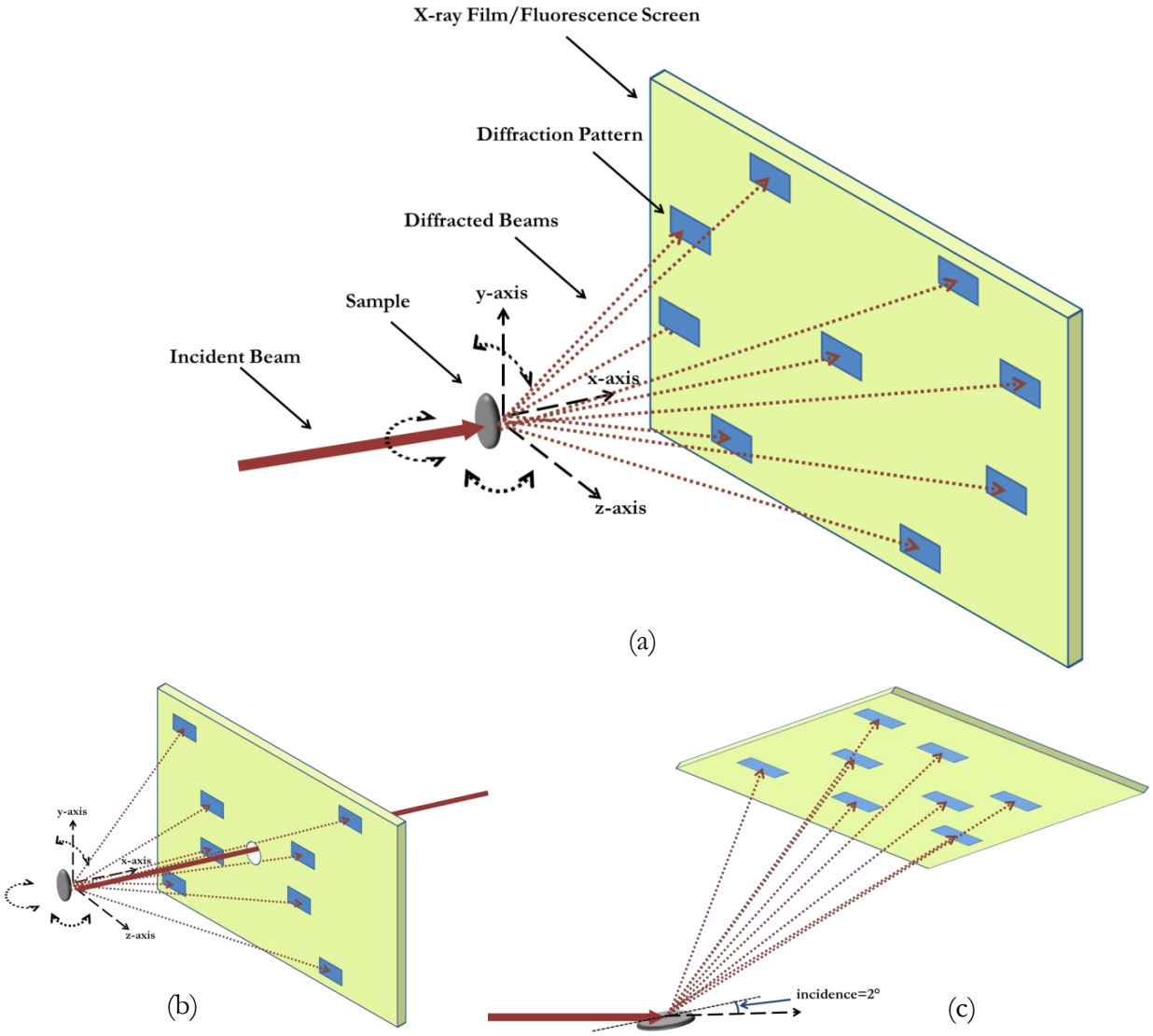

Figure 2-2 Illustrations of the three different experimental setups commonly used in SWBXT—a) Transmission; b) Back-reflection; c) Grazing-incidence reflection.

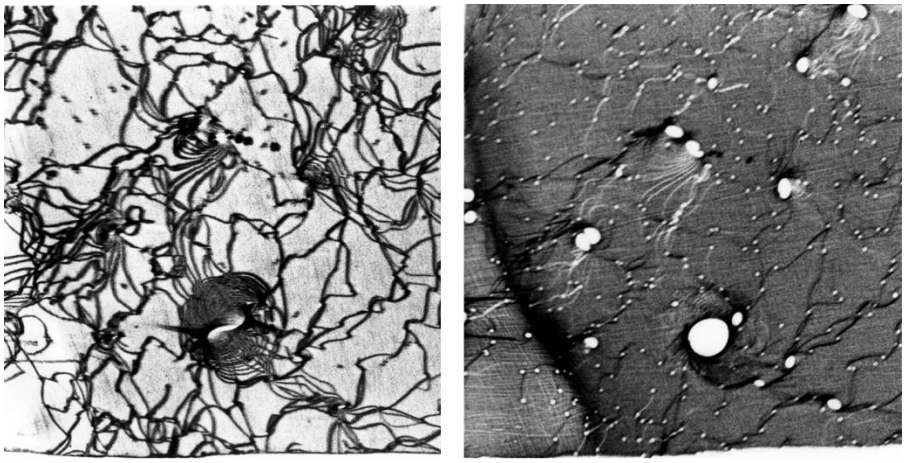

(a) (b)

Figure 2-3 (a) typical transmission X-ray topograph (g=11-20, λ=0.59Å) showing BPDs in comparison with (b) typical back reflection X-ray topograph (g=00024, λ=1.24Å) showing SDs and MPs. Small white dots are elementary TSDs and large white dots are MPs in (a) and the curved black lines in (b) are BPDs. (Topographs originally published in Ref. [99]).

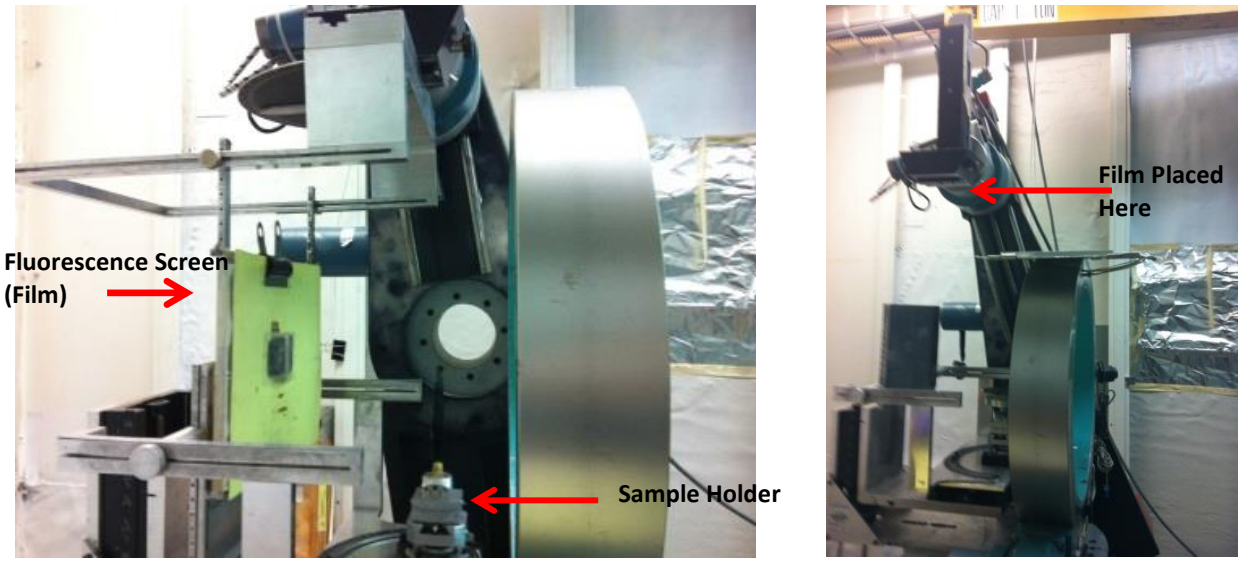

(a) (b)

Figure 2-4 Pictures taken at the NSLS X-19C beamline showing the experiment setups for a) transmission topography and b) grazing-incidence topography.

Films used to record the diffracted images in our experiment are Agfa Structurix D3-SC films. The exposure time varies depending on the arrangements mode involved and the sample's absorption capability of the X-ray. For the grazing-incidence reflection, the typical exposure time is 8~15s. Chemicals used to process the X-ray films are Kodak D19 developer & fixer combination. The developing time is around 15s, and the fixing time about 10 min.

2.1.3 Contrast and Resolution in X-ray Topography

As long as the crystal is not perfect, contrast variations should be observed from each spot on the Laue diffraction patterns. Those contrast variations resulting from the differences in the intensity of diffracted beam, which reveal the local diffracting power discrepancy that arises from the local crystal lattice distortion, are the most important information manifested on the topographs. Both qualitative and quantitative results, such as different defect types, the line direction and the sense and magnitude of the Burgers vector of an individual dislocation could be obtained by detailed analysis of contrast variation of the topographs under different diffraction conditions.

Regarding the interpretation of X-ray topographs, two fundamental contrast mechanisms are involved—orientation mechanism and extinction mechanism. Extinction mechanism, described by means of kinematical [100] and the dynamical [100, 101] theories of X-ray diffraction, can be further divided into three different types in terms of different diffraction conditions that determined by the absorption condition, defined as μt, where μ is the linear absorption coefficient of the examined material and t is the sample thickness through which the incident beam transverse. Those three ones are recognized as direct image contrast ($\mu t<1$), dynamical contrast ($\mu t>6$), and intermediary contrast ($1< \mu t<6$), and the corresponding images arisen by those contrasts are called direct image, dynamic image and intermediary image, respectively.

The orientation contrast in white beam topographs simply results from the overlap and separation of diffracted beams induced by the misorientation of the crystal lattice. Fig. 2-5 illustrates clearly how this contrast originates.

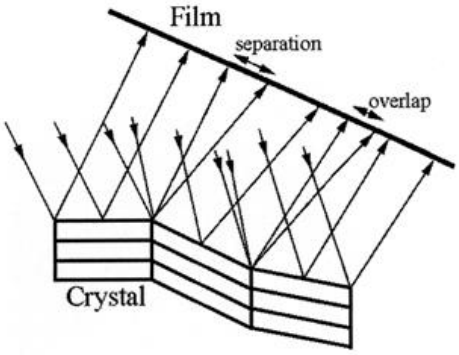

Figure 2-5 Illustration shows how the orientation contrast arises from the misorientated regions when exposed to the continuous beam [81].

Under low absorption conditions ($\mu t<1$), the direct image contrast dominates the topograph. When μt gets larger but not exceeds five, the topographs are composed of all three types of images, and for even higher absorption conditions, say $\mu t > 6$, the dynamical contrast makes the major contribution.

One of the most important applications as a result of the deep understanding of the contrast in topographs under different diffraction conditions is to determine the Burgers vector of dislocations via ***g.b*** analysis. ***g*** is the reflection vector perpendicular to the diffracted planes and ***b*** is the Burgers vector of the dislocation. As is well known from the work of A. Authier, the direct image width *w* of a dislocation in SWBXT images can be estimated as [102]:

$$w \approx \boldsymbol{g} \cdot \boldsymbol{b}\xi_g/2\pi$$

ξ_g refers to the extinction distance in the equation above. Equation above provides the critical invisibility criterion for direct images of dislocations in SWBXT—***g.b***, indicating that in the case of ***g.b***=0, dislocations are out of contrast, meaning that they are invisible on topographs. Fig. 2-6 shows selected same region of the transmission topography images of a sapphire (α-Al_2O_3) wafer under six different reflection conditions. By taking ***g.b*** analysis according to the contrast variation in those images, both the Burgers vector and the type of certain dislocations can be determined.

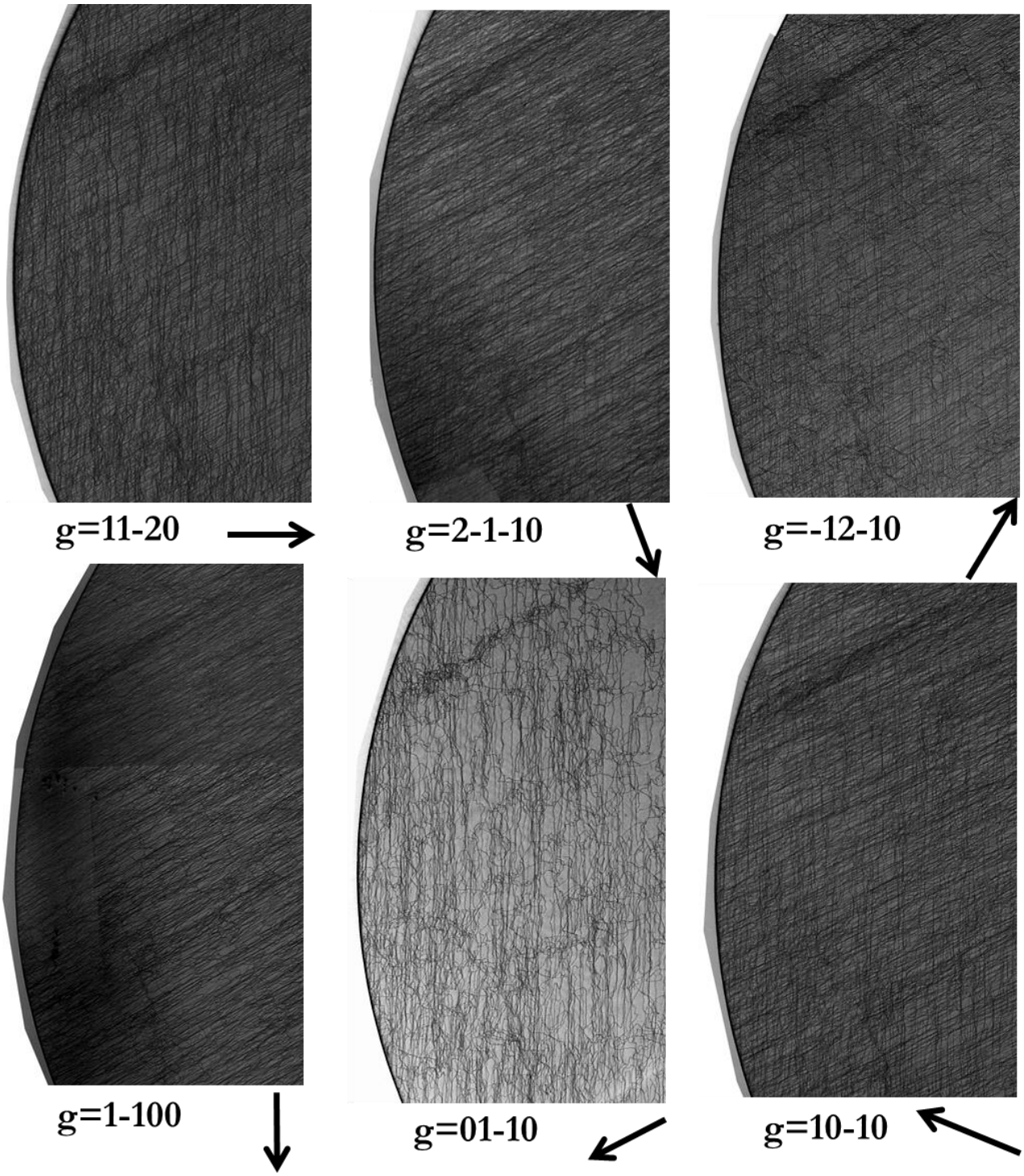

Figure 2-6 Selected same region of the transmission topography images of a sapphire (α-Al_2O_3) wafer under six different reflection conditions. As can be observed from the images, dislocation lines along [1-100] direction disappear on the image whose reflection vector is $\boldsymbol{g}$=<01-10> and those dislocations aligning with [01-10] directions disappear on the $\boldsymbol{g}$= <1-100> image. Through $\boldsymbol{g.b}$ analysis, they have Burgers vectors $\boldsymbol{b}$=1/3<2-1-10> and $\boldsymbol{b}$=1/3<11-20>, respectively. Both of them have Burgers vector perpendicular with their line directions and thus they are both pure edge dislocations.

The spatial resolution in topography is given by [81]

$$R = SD/C$$

where R is the effective resolution, S is the maximum source dimension in the direction perpendicular to the plane of incidence, D is the specimen-film distance, and C is the source specimen distance. The equation tells us that in terms of the beam size, it is the height of the beam rather than the width that takes effects on the resolution of the topography images.

2.2 Molten Potassium Hydroxide Etching

Chemical etching is another common surface method used to reveal the defects of crystal substrates. As the crystal is subjected to an environment where reaction take place between the chemical and the sample, the rate at which atoms are removed from the near-perfect region and from the region containing defects are different, resulting in certain etch pits that gives information on the characteristics of the local defects. Wide band gap semiconductors, like SiC, for example, ususally show high resistance to the majority of the etching systems conventionally applied for other compound semiconductors. Studies indicate that molten potassium hydroxide (KOH) etching is an effective way to detect the defects near the surface of those materials [103-106]. Usually the samples are immersed pure molten KOH at a temperature between 450 °C to 600 °C for a appropriate time (typically~10min). Studies on the correspondence between the etch pits and the nature of defects have been carried out by many research groups [107-109].

2.3 Nomarski Optical Microscope

The Nomarski Optical Microscope, also well-known as the differential interference-contrast (DIC) microscope or the polarization interference contrast microscope, is widely used as a surface characterization technique to enhance the contrast in thin transparent samples. It works in the principle of enhancing the image contrast by using the phase difference occurring during the process when light passes through the material with different refraction values, or varying thickness. As for the characterization of semiconductor substrates, etched crystalline features could be observed in a striking appearance with color variation (shadow) and a pseudo three-dimensional effect. Two illumination modes are involved in observing samples under DIC microscope. The transmission modes allow the lights go through the specimen and all the features inside the sample body could be studied, while the reflection mode help to focus on a thin plane section near the surface of a thick sample.

3 RESULTS & DISCUSSION

3.1 Quantitative Comparison between Dislocation Densities in Offcut 4H-SiC Wafers Measured Using SWBXT and Molten KOH

3.1.1 Background

Though great development has been made in both the crystal growth and the device fabrication of SiC, the widespread commercialization of this material is still hindered by relatively high densities of structural defects that exert negative influence on device performance as well as lifetime. Therefore it is of great importance to develop precise visualization techniques for those defects in order to understand their growth and propagation mechanisms, and to eventually reduce or even eliminate the densities of these defects.

A wide range of techniques have been used to study the distribution, arrangement, and density of dislocations. Regarding the assessment of dislocation density, two major techniques—molten KOH etching and X-ray topography are preferred. Though by nature destructive, molten KOH etching is popular in dislocation density assessment due to its low cost, ease of accessibility, and easy operation. However, it suffers the drawback of only being able to reveal the structural property near the etched surface. Additionally, problems arise when attempts are made to relate etch pits densities (number of etch pits per unit area, $/cm^2$) to the true dislocation density (total length of dislocation lines per unit volume, cm/cm^3) when the dislocations in question are far from being perpendicular to the etched surface.

Fig.3-1 (a) shows a Nomarksi Interference Contrast (NIC) optical image of a selected area on an etched commercial PVT-grown 4^o offcut 4H-SiC wafer. As for the samples used in this experiment, three different kinds of etch pits pattern are observed. The large and small hexagonal etch pits correspond to TSDs and TEDs, respectively, while the scallop-shell-shaped pits correspond to BPDs. Both TSDs and TEDs have line directions roughly perpendicular to the (0001) plane while BPDs have the line directions contained in the basal plane, as their name would indicate. The difference in size between the TSD and TED pits, while maintaining the same symmetrical shape can be explained by their different Burgers vector magnitudes and similar line directions [110]. Occasionally, TED etch pits may deviate slightly from the symmetrical hexagonal shape due to the

offcut angle [111]. The correlation between the etch pits features and corresponding dislocations are confirmed by ***g.b*** analysis of the X-ray topography images.

Synchrotron white beam X-ray topography (SWBXT), on the other hand, as a non-destructive characterization technique, provides a true three dimensional view of the overall defect distribution in the volume imaged. For BPDs whose Burgers vector is 1/3<11-20>, when taken in transmission topography with ***g***=<11-20>, ***g.b*** yields non-zero results and thus all the BPDs are in contrast on the (11-20) transmission SXRT images.

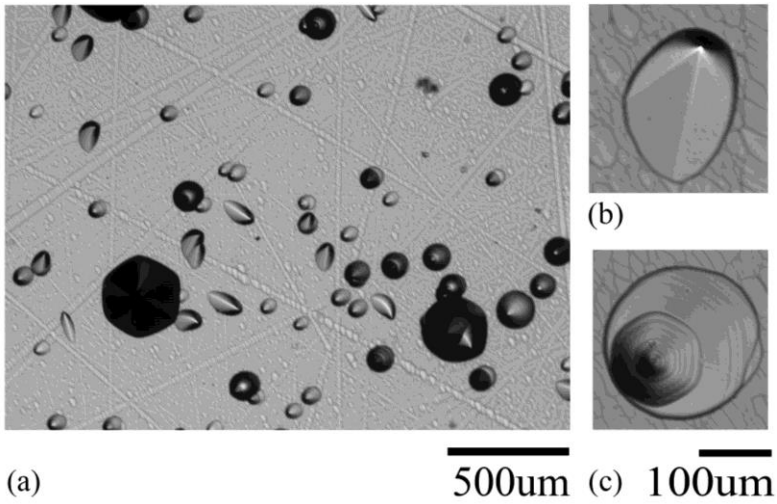

Figure 3-1 A Nomarski Interference Contrast optical image showing a selected area on an etched Si-face of a commercial PVT-grown 4° offcut 4H-SiC wafer (a). Three types of etch pits are observed—scallop-shell-like shaped etch pits corresponding to BPDs (b), large hexagonal etch pits to TSDs, small hexagonal etch pits to TEDs (c)

3.1.2 Experimental Procedure

Two commercially available 4H-SiC substrates from Dow Corning grown by the physical vapor transport (PVT) technique with an 4° offcut angle toward the [11-20] direction were etched on Si-face in molten potassium Hydroxide (KOH) before synchrotron white beam X-ray transmission topographs using 11-20 reflection were recorded. The doping level for those samples is 3e18. For each wafer, eight 1.8mm×2.3mm areas were randomly chosen from the topography images while corresponding optical images showing the etch pits were recorded from the same areas using Nomarksi microscopy (Nikon ECLIPSE E600 POL) (Fig.3-2(a)-(b)). BPD densities are calculated and quantitatively compared by etch pit counting and by line length measurement from the topography images.

3.1.3 Results & Discussions

Fig. 3-3 (a) & (b) are histograms showing the discrepancy for the two tested wafers. Wafer 1, with a thickness of 380μm, bears a BPD density calculated from etch pit counting varying from 193/cm^2 to 483/cm^2, while the value calculated from topography images varying from 4051cm/cm^3 to 8092cm/cm^3. The average ratio between the BPD density obtained from topography and etch pit analysis is around 18. For Wafer 2, with the thickness of 435μm, this ratio turns out to be 20. In order to reveal the underlying reason for these disparities in value, a close inspection of how BPD density is calculated in each technique is required.

By calculating dislocation density by etch pit counting, it is assumed that the following equation is justified.

$$\rho = \frac{L}{V} = \frac{N_d \times l}{A \times t} = \frac{N_e}{A} \qquad (1)$$

L represents the total length of dislocation lines in selected volume V, while l is the average length of dislocation lines. N_d stands for the total number of dislocation lines in volume V and the total number of etch pits on the etched surface of area A is denoted as N_e. t is the thickness of the wafer. Obviously the original definition of dislocation density—total length of dislocation line per unit volume, is not strictly followed during this calculation process. The equation above is only justified when a) N_d equals N_e and meanwhile b) the average length of dislocation line is almost the same as the wafer thickness. While these assumptions are justified for threading dislocations whose line directions are nearly parallel to the c-axis like TSDs and TEDs, the assumptions are most definitely not valid for the case of BPDs (Fig. 3-4 (a)).

Fig. 3-2 shows an SWBXT image ((a)) and NIC image of etch pits ((b)) taken from the same area of an etched 4H-SiC wafer. Though BPD1 and BPD2 can be observed in both ((a)) and ((b)), BPD3, going through the sample body without intersecting the top surface can only be seen in SXRT image. No corresponding etch pit is found in the optical image.

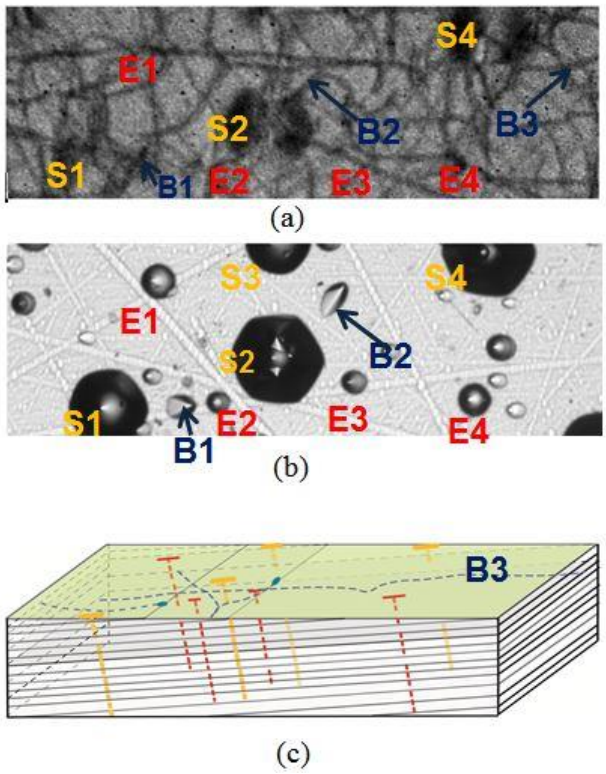

Figure 3-2 SWBXT image (a) and NIC image of etch pits (b) taken from the same area of a pre-etched 4H-SiC wafer. The illustration (c) demonstrates how threading dislocations (S1-S4: TSDs; E1-E4: TEDs.) and BPDs (B1-B3) are oriented in the sample.

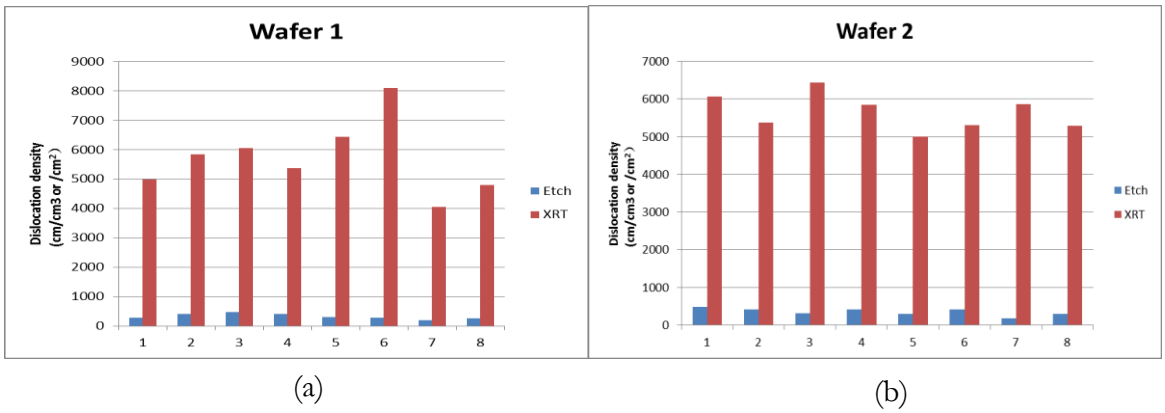

Figure 3-3 Histograms showing the discrepancy of BPD densities obtained from etch pit counting and SXRT image line length measurement for eight 1.8 mm×2.3mm areas on each of the two commercial 4H-SiC wafers with different thickness.

As illustrated in Fig. 3-4 (b), only those BPDs that lie within the wedge ABCDEF might have a chance to intersect the top surface, like BPD1 and BPD2. On the other hand, BPD4 and BPD5 do not emerge on the top surface and therefore corresponding etch pits cannot be observed.

Even for those BPDs that lie within the wedge, not all of them will intersect the top surface. For example, BPD3 does not emerge on the top surface.

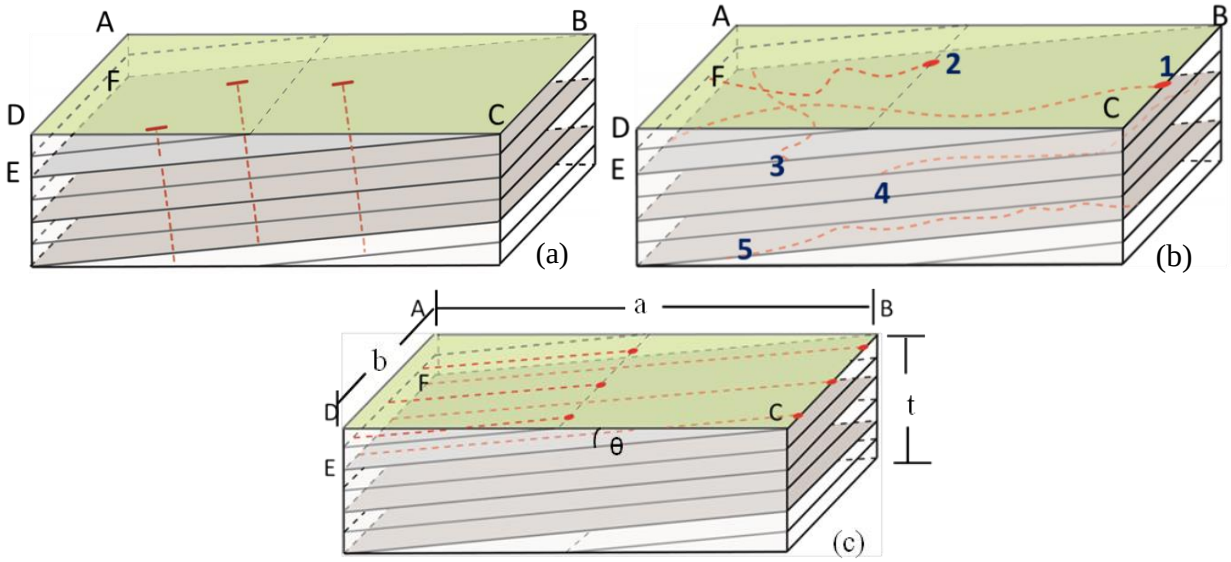

Figure 3-4 Schematic diagrams giving a rough view showing the morphologies of (a) threading dislocations and (b) BPDs inside a wafer. The grey-shaded planes are (0001) basal planes that have an offcut angle of θ inclining towards the top surface. (c) illustrates a simplified model where BPDs are considered as straight lines distributed uniformly in the selected volume. *a* and *b* refer to the dimensions of the selected etched area and t stands for the sample thickness

To further reveal the magnitude of this value disparity, an analytical model is proposed based on a rough assumption that all the BPDs are distributed uniformly as straight lines within the selected sample bulk (Fig. 3-4 (c)). This is reasonable if the selected sample volume is much smaller than the whole wafer. Considering such a uniform BPD distribution, the ratio of the number of all BPDs in the selected volume to the number of etch pits should be less than or equal to (assuming the ideal condition that all the BPDs within the wedge intersect the etched surface) the ratio of the volume of the whole selected rectangular bulk to that of the wedge, namely:

$$\frac{N}{N_e} \geq \frac{a \times b \times t}{\frac{1}{2} a \times b \times \frac{a}{ctg\theta}} = \frac{2t \times ctg\theta}{a} \qquad (2)$$

As illustrated in Fig. 3-4(c), *a* and *b* refer to the dimensions of the selected etched area and θ is the offcut angle. And thus the ratio of the true BPD density in volume $a \times b \times t$, denoted as ϱ, to the density obtained from etch pit counting in the area $a \times b$, denoted as ϱ_e, is given in Equation (4) as below:

$$\frac{\rho}{\rho_e} = \frac{N \times L}{N_e \times t} \geq \frac{2 \times L \times ctg\theta}{a} \qquad (3)$$

When considered as straight lines, the average length of BPD in the wedge is $a/(2\cos\theta)$. Since the BPDs are naturally curving around on the basal planes (Fig. 3-4 (b)), making their average length larger than the value above, meaning:

$$L > \frac{1}{2}\frac{a}{\cos\theta} \qquad (4)$$

Combining Equation (3) and (4) leads to the safe conclusion that the ratio of the real BPD density of the sample to the value calculated from etch pits counting is larger than $1/\sin\theta$. For example, if the offcut angle is 4°, which is true for both wafers used in this experiment, this ratio is expected to be larger than 14 ($1/\sin 4^{o}$). The experiment results demonstrated before are found to be in good agreement with this model prediction (Fig. 3-4).

3.1.4 Summary

Dislocation etching techniques are relatively economical and straight forward to implement and have been used very successfully to reveal dislocations in SiC. However, one can encounter problems when converting measures of etch pit density (number of lines crossing unit area) to true dislocation density (line length per unit volume) since 1) etching only reveals the defects that intersect the sample surface and 2) the conversion from etch pit density to true dislocation density wrongly considers the average length of BPDs as almost the same as the sample thickness. Unless the dislocations are arranged in a fully three dimensional, homogeneous network, true dislocation densities inferred from etch pit counts are always going to be a function of the plane chosen and can yield different values depending on the orientation of that plane. Therefore the value of BPD density obtained by etch pit counting is potentially very misleading. On the other hand, X-ray topography, by nature providing a true 3-D view of the overall defect distribution reveals all dislocations not only intersecting the surface but also lying inside the wafer. It gives more precise results when used in density assessment.

3.2 Defects Analysis of Sublimation & Recondensation Grown AlN Single Crystals via SWBXT

3.2.1 Background

Due to the material's outstanding intrinsic properties including high breakdown field, large bandgap, and high ultraviolet transparency, aluminum nitride (AlN) single crystal substrates have shown promising application for a wide range of electronic devices operated under extreme conditions like high power switches and high frequency microwave devices, as well as for the optoelectronics operated in ultraviolet radiation range such as UV LEDs/LDs, solar blind UV light detectors.

The growth of AlN from the vapor phase has been proved to be the most effective way to produce high quality single AlN crystals. Both self-seeded and foreign material seeded techniques have been utilized for bulk AlN growth [75-78]. Fig.3-5 shows pictures displaying two c-orientation AlN single crystal boules grown by PVT technique. They are both N-polar self-seeded in an environment where growth temperature is higher than 2200 °C. Both well-defined c- and m- plane facets are noticed on the two boules. Significant increase in diameter with growth can be observed.

Compared to SiC, the more mature wideband gap semiconductor that has longer development history, the main limitations for AlN lie in both the small dimensions of the wafer and the relatively high defect density. Larger wafer size would considerably reduce the prime cost and single crystal AlN substrates with relatively low dislocation density display the capacity to substantially improve the performance and lifetime of nitride-based devices compared to prevalent device technologies based on sapphire and silicon carbide substrates, especially for device designs requiring high Al compositions. Hence, the larger diameter wafer growth and higher crystal quality control remain the two major challenges which attract both researchers and industry.

Since it is of great significance to help improve the crystal quality of AlN, effective characterization technique is also in high demand. SWBXT help map the defect types and their distributions, in order to gain insight into defect nucleation mechanisms and their propagations. The main goal is to help minimize or even get rid of those defects by optimizing the growth condition and developing better growth strategies.

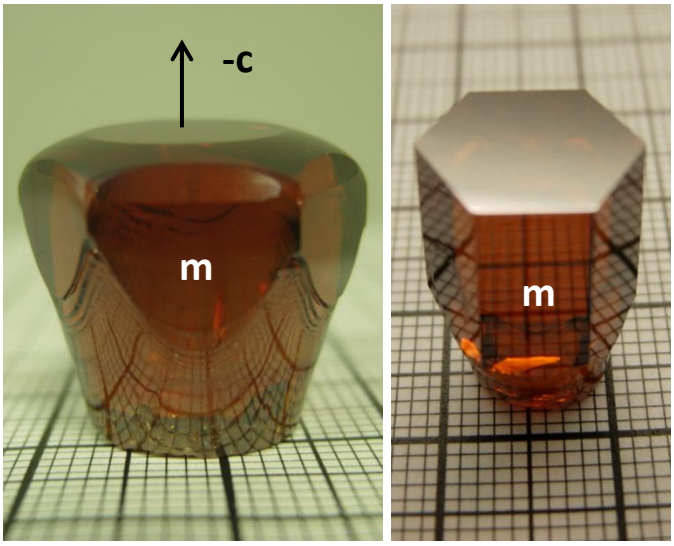

Figure 3-5 c-orientation AlN single crystal boule grown by PVT technique from N-polar single crystal seeds. Well-defined c- and m- plane facets are marked. Significant increase in diameter with growth can be observed. Provided courtesy of Hexa Tech Inc.[112].

3.2.2 Experimental Procedure

The transmission topography has been carried out on six PVT-grown AlN wafers in 3×{11-20}&3×{1-100}six reflections. Grazing-incidence reflection topography has also been taken for some selected areas when necessary. Nomarski optical microscopy is used as a supplementary means to help with the defects analysis.

As explained in Fig. 2-5, the orientation contrast of the LAGB is merely the result of the diffracted beam separation arising from the misorientated regions. From the Fig. 2-5 illustration it can be predicted that the larger the sample-to-film distance is, the wider the separation would be, and thus the wider boundary lines in the topograhs would appear. To prove that the feature observed in the topograh is LAGB, transmission topography experiment has been carried out for the same area three times at different sample-to-film distances.

3.2.3 Results & Discussion

Most of the defects observed in the sublimation-recondensation grown AlN wafers are similar to those studied in the PVT grown SiC wafers. Besides basal plane dislocations (BPDs), threading edge dislocations (TEDs) and threading screw dislocations (TSDs), low angle grain boundaries (LAGBs) are one of the most noticeable features in the AlN samples.

Fig. 3-6-Fig. 3-11 display the defect distribution of the six AlN samples shown in the transmission topography images. Though in total six different reflections are taken for each sample, only the **g**=(11-20) reflection images are demonstrated here as examples. Overall, the samples are of pretty high quality with heterogeneous distribution of defects. In Sample1-3 & Sample5, certain areas have been picked up where the dislocation density is as low as ~$10/cm^2$ or even zero. LAGBs are observed in each individual sample. Fig. 3-8 gives the example illustrating the two different types of LAGBs. Type I LAGB is composed of a-type TEDs with Burgers vector 1/3<11-20>, while Type II LAGB is formed by BPD accumulation. Fig 3-8 (b) is a grazing-incidence reflection topograph of certain area containing part of the Type I LAGB, in which the black spots represent TEDs. Besides, in transmission topography images, BPDs, shown as black curved lines due to the stress often caused by thermal factors and TEDs, shown as very short lines are observed to tend to array adjacent to LAGBs. For type I LAGBs, the arrays of TEDs composing them are either replicated from the seed or formed to separate regions growing with slightly different rotations. The type II LAGB formation, on the other hand, is related to initial growth stages and could be due to competition between the main crystal and secondary nucleated grains slightly misoriented with respect to the main crystal. BPDs are nucleated from the boule edges due to thermal gradients and forming Type II LAGB due to stress concentration. Though resulted from the accumulation of dislocations, boundaries can also hamper the dislocations' further movements, as observed in Sample5&6 (Boundary B in Fig.3-10&Boundary B in Fig. 3-11). The frequent occurrence of inclusions is also a big concern in the PVT-grown AlN wafer. It might be related to the dislocation initial growth during the crystal growth process. Boundaries and inclusions can sometimes be seen directed under the optical microscopy examination (Fig. 3-6 (b) and Fig. 3-9 (b)&(c)).

Fig. 3-10 (b)-(d) provide the verification that the features D&C in Fig. 3-10 (a) are LAGBs. These three are (1-100) transmission topography images taken from the same area D&C occupy in the sample. Different sample-to-film distance—20 cm, 30 cm, and 40 cm are set for (b), (c), and (d), respectively. They give the sound proof that the contrast of features D&C are merely orientation contrast introduced by the diffraction beam separation due to the geometrical misorientation, by showing that as the SFD increases, the width of the boundary image also enlarges. Recall that the spatial resolution of the topography has been determined by:

$$R = SD/C$$

where R is the effective resolution and D is the sample-to-film distance. This accounts for the reason why as the sample-to-film distance increases from (b) to (d), the image gets more and more blurry.

A helical loop dislocation that might be resulted from annealing process is found in Sample6 (Fig. 3-11 (b)-(g)). **g.b** analysis reveals that its Burgers vector is 1/3 <-12-10>.

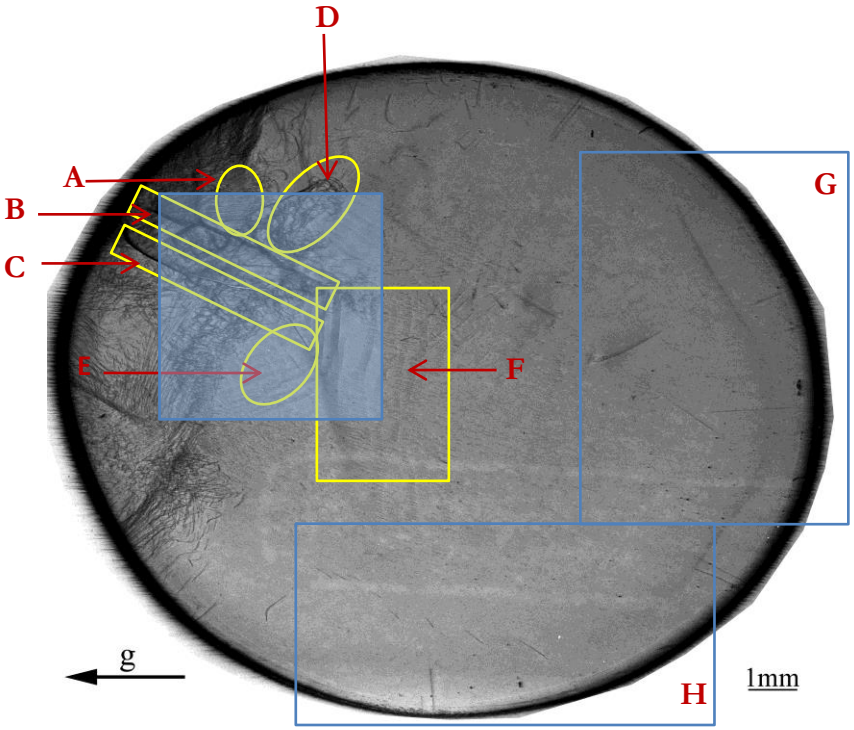

(a)

(b)

Figure 3-6 Defects distribution analysis of AlN Sample1 on the transmission topography ((a)) with ***g***= (-1-120) and the corresponding transmission optical image ((b)). A: Screw dislocations with Burgers Vector ***b***=1/3<11-20>; B&C: LAGBs; D&E: BPDs; F: threading dislocation arrays; G&H: high quality regions on the wafer where the dislocation density is as low as about 100/cm^2. The shadowed square region shows that LAGBs and TDs are visible in the optical image due to the decoration with vacancies (/impurities).

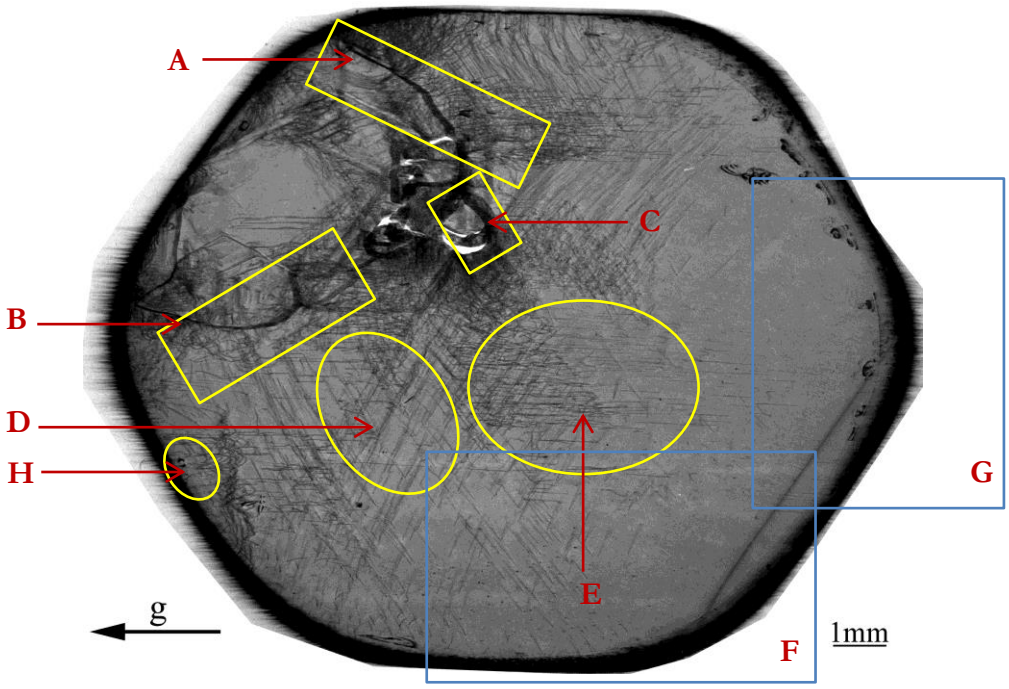

Figure 3-7 Defects distribution analysis of AlN Sample2 on the transmission topography with **g**= (-1-120). A, B & C: LAGBs; D: screw dislocation with Burgers vector ***b***=1/3 <2-1-10>; E: screw dislocations with Burgers vector ***b***=1/3<11-20>; F: high quality region on the wafer where the dislocation density ~1000/cm^2; G: high quality region on the wafer where the dislocation density ~100/cm^2. H: inclusion.

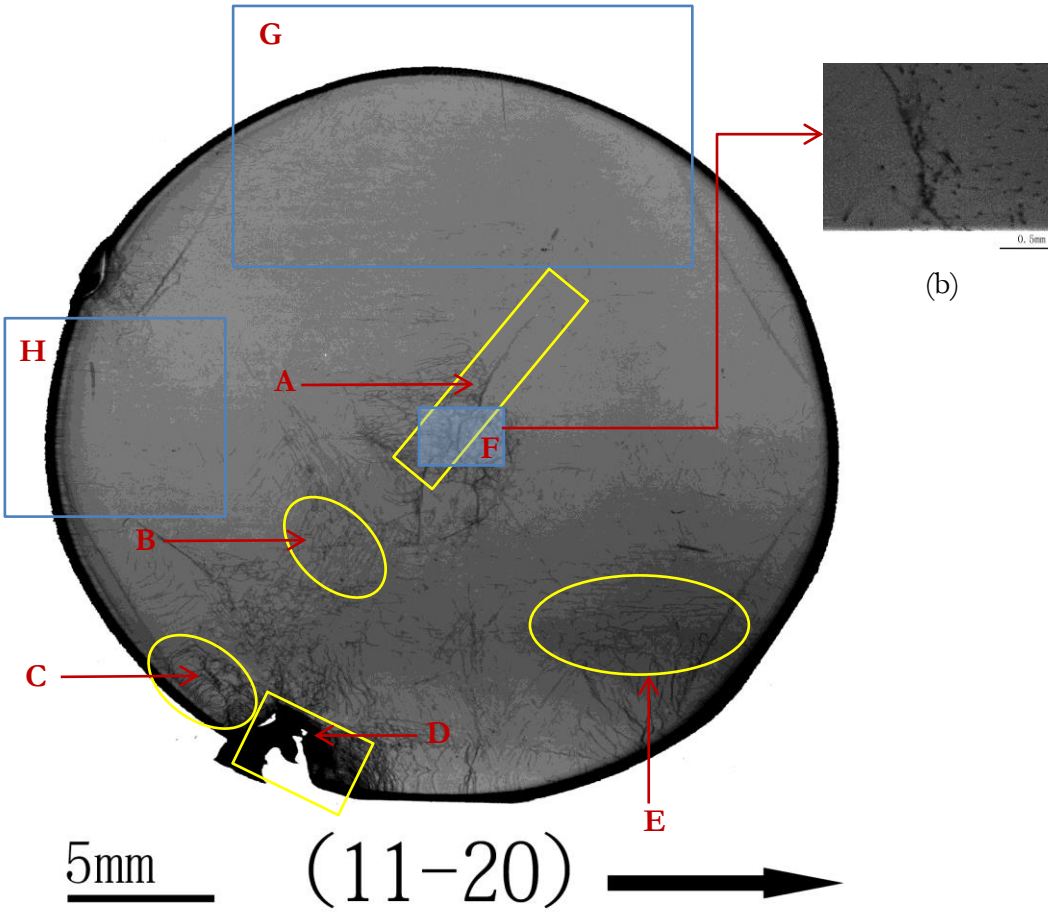

Figure 3-8 Defects distribution analysis of AlN Sample3 on the transmission topography ((a)) with **g**= (11-20) and grazing-incidence topography image for certain selected area ((b)). Two different types of LAGBs (A—type I and D—type II) are observed; B: screw dislocaitonss with Burgers vector ***b***=1/3 <-12-10>; C: BPDs adjacent to the type II LAGBs; E: screw dislocations with Burgers vector ***b***=1/3<11-20>; F: reflection topography image showing that threading dislocations accumulate together composing the type I LAGB; G&H:high quality region on the wafer where the dislocation density ranges from ~100/cm^2 to even dislocation-free.

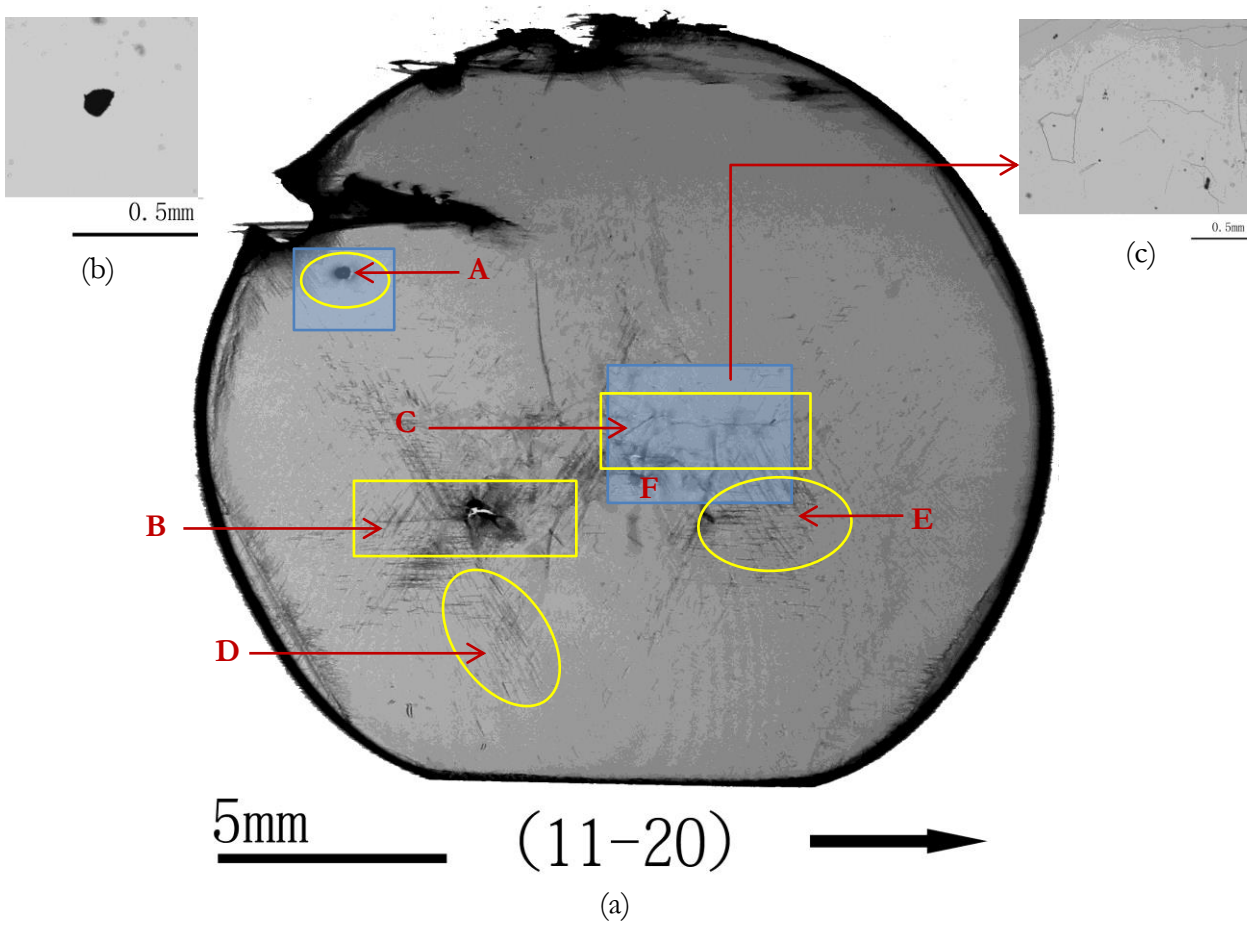

Figure 3-9 Defects distribution analysis of AlN Sample4 on the transmission topography ((a)) with **g**= (11-20) and corresponding Nomarski optical images for a closer look at certain selected features ((b)). A: inclusions; B&C: LAGBs and the shadowed area F shows that they are visible in the optical image ((c)); D: screw dislocations with Burgers vector ***b***=1/3 <2-1-10>; E: screw dislocations with Burgers vector **b**= 1/3 <11-20>.

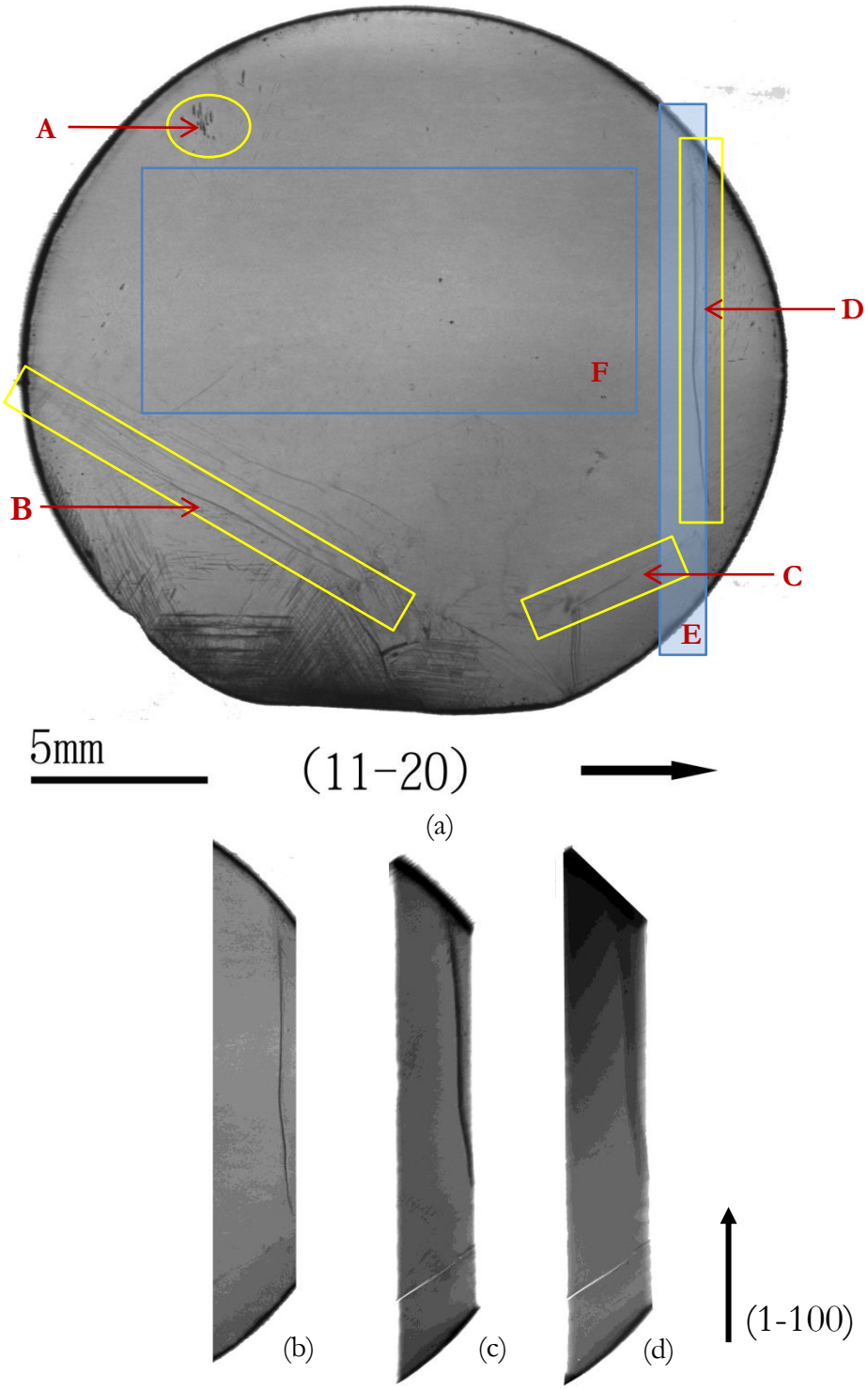

Figure 3-10 Defects distribution analysis of AlN Sample5 on the transmission topography ((a)) with **g**= (11-20). A: inclusions; B, C&D: LAGBs. Transmission topography in (1-100) reflection has been taken for the shadowed area E at different sample-film distances (SFD)—20cm ((b)), 30cm ((c)), and 40cm ((d)). ((b))-((d)) demonstrates clearly that as the SFD increases, the width of the boundary image also enlarges. F: high quality area with dislocation density 0~100 /cm².

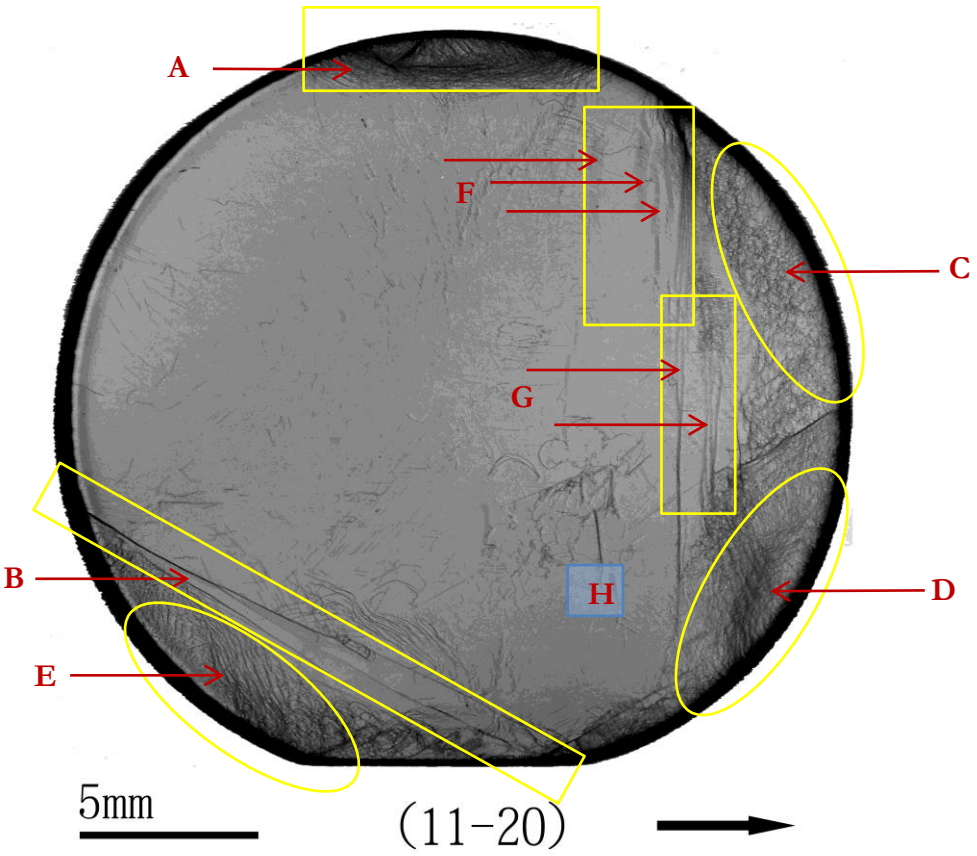

(a)

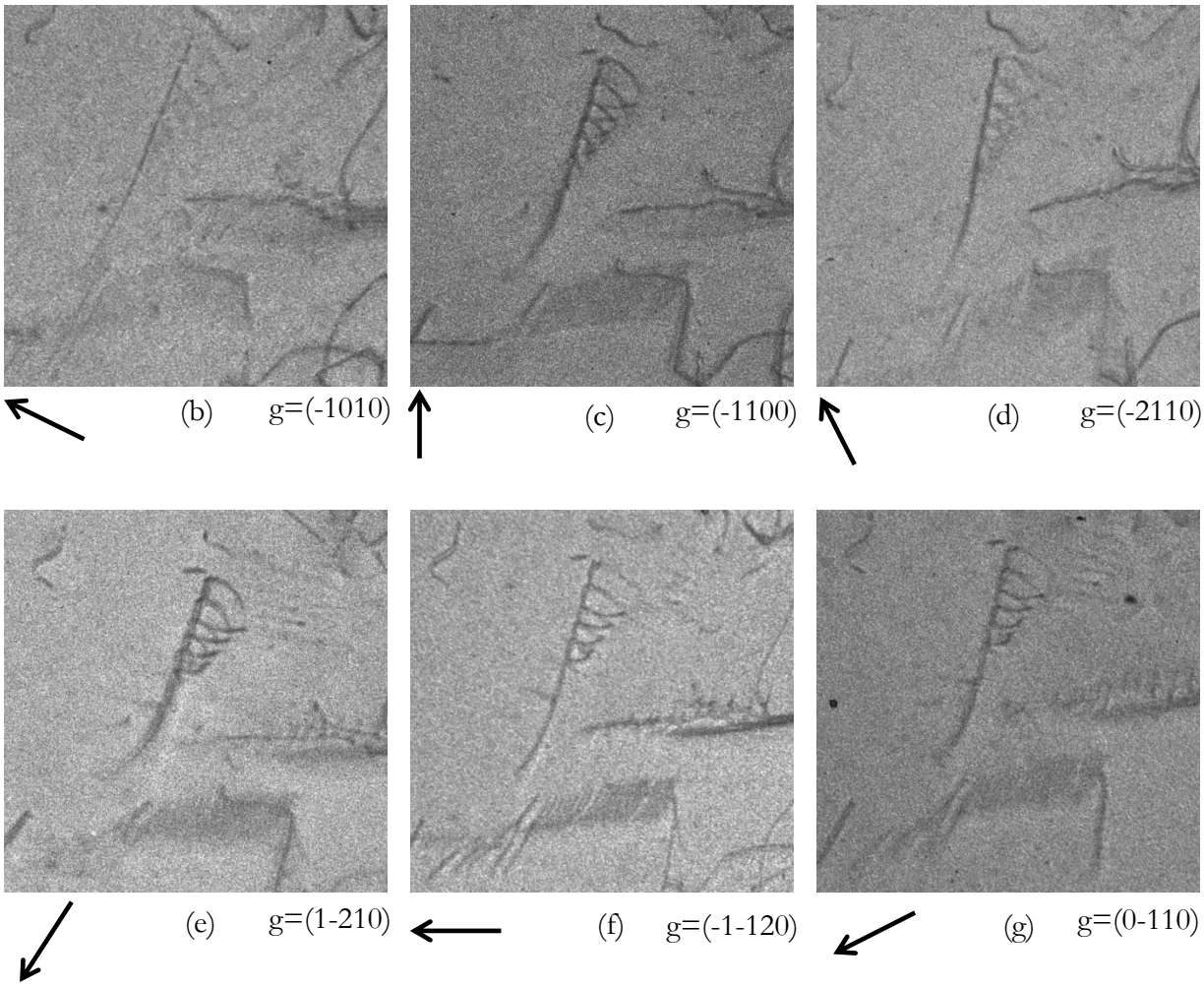

Figure 3-11 Defects distribution analysis of AlN Sample6 on the transmission topography ((a)) with ***g***= <11-20> and magnified images in six different reflections ((b)-(g)) of the helical loop dislocation found in the sample. A&B: LAGBs (type II); C, D&E: BPDs; F&G: threading dislocation arrays; H: helical loop dislocation with a Burgers vector 1/3<-12-10>.

3.2.4 Summary

Overall, these AlN substrates are in high quality, characterized by low dislocation densities with large areas exhibiting high crystalline perfection. The major defects observed include LAGBs, threading dislocations, BPDs and inclusions. Two different types of LAGBs are studied. One is composed of arrays of TEDs that either replicated from the seed or formed to separate regions growing with slightly different rotations and the other is formed mainly by BPDs accumulation due to stress concentration.

4 CONCLUSION

Synchrotron white beam X-ray topography has been demonstrated to be a very effective technique used for the characterization of wide bandgap semiconductor single crystals. Different types of defects are observed and their distributions are clearly mapped. By contrast analysis, lots of information such as line direction and magnitude and sense of Burgers vector of individual dislocation are able to be obtained. Quantitative information like overall dislocation density of the crystal is also accessible. The origin and propagation mechanism of some defects can be postulated via detailed analysis.

For the two representatives of the class of wide bandgap semiconductors—SiC and AlN, various challenges still remain for their crystal growth, characterization and process development. Those challenges include uniform, reproducible electrical properties, defect reduction or even elimination, wafer diameter expansion and device structure design optimization. In the future, more work need to be done in regarding with the further understanding of structures and properties of different defects in the substrates, epilayers and also devices. To get a deeper view of the formation and propagation mechanism of the defects is of great help in controlling the growth of them and reducing their densities in crystals. The future breakthrough of better devices depends on the development and practical commercialization of low dislocation density, or even dislocation-free crystal growth.

REFERENCES

[1] J. B. Baliga, IEEE Electron Dev. Lett. **10** 455 (1989).
[2] J. B. Casady, R. W. Johnson, Solid-St. Electron, **38** pp.1409-1422 (1996).
[3] B. Ozpineci and L. M. Tolbert, *Comparison of Wide Bandgap Semiconductors for Power Electronics Applications*, ORNL/TM-2003/257, UT-Battelle, LLC, Oak Ridge National Laboratory, (2003).
[4] A. R. Hefner, R. Singh, J. Lai, D. W. Berning, S. Bouche, and C. Chapuy, IEEE Transactions on Power Electronics, pp. 273–280 (2001).
[5] Y.-F. Wu, A. Saxler, M. Moore, R. P. Smith, S. Sheppard, P. M. Chavarkar, T. Wisleder, U. K. Mishra and P. Parikh, IEEE Electron Device Lett. **25** 117 (2004).
[6] P. G. Neudeck, R. S. Okojie, and Liang-Yu Chen, Proc. IEEE, **90** pp.1065-1076 (2002).
[7] T. Ericsen, Proc. IEEE, **90** pp.1077–1082, (2002).
[8] K. C. Reinhardt, M. A. Marciniak, Proc. 3rd Int. High-Temperature Electronics Conf., pp. I.9-I.15 (1996).
[9] P. L. Dreike, D. M. Fleetwood, D. B. King, D. C. Sprauer, and T. E. Zipperian, IEEE Transactions A **17** 594 (1994).
[10] C. S. White, R. M. Nelms, R. W. Johnson, and R. R. Grzybowski, Thirty-Third IAS Annual Meeting, IEEE, **2** 967 (1998).
[11] J. Palmour, R. Singh, R. C. Glass, O. Kordina, and C. H. Carter, Power Semiconductor Devices and IC's-ISPSD'97, pp. 25 - 32 (1997).
[12] P. G. Neudeck, R.S. Okojie, and Liang-Yu Chen, Proc. IEEE, **90** 1065 (2002).
[13] R. S. Okojie, A. A. Ned, G. Provost, and A. D. Kurtz, Proc. 4th Int. High Temperature Electronics Conf. 79 (1998).
[14] P. G. Neudeck, "600 °C Digital Logic Gates", NASA Lewis 1998 Research & Technology Report (1999).
[15] S. Strite and H. Morkoc, J. Vac. Sci. Technol. B, **10** 1237 (1992).
[16] Robert F. Davis, Proc. IEEE, **79** 702 (1991).
[17] Max N. Yoder, IEEE Transactions on Electron Devices, **43** 1633 (1996).
[18] A. Verma and P. Krishna, Polymorphism and Polytypism in Crystals(Wiley, New York 1996).
[19] N. W. Jepps and T. Page, in Progress in Crystal Growth and Characterization, ed. By P. Krishna **7** pp. 259-306 (Pergamon, Oxford, 1983).
[20] J. A. Powell, P. Pirouz and W. J. Choyke, in Semiconductor Interfaces, Microstructures and Devices: Properties and Applications, ed. By Z.C. Feng (Hilger, Bristol, 1992).
[21] P. G. Neudeck, "Silicon Carbide Technology", in The VSLI Handbook.2nd edition, (2006).
[22] Hiroyuki Matsunami, Tsunenobu Kimoto, Mater. Sci. and Eng., R20 pp.125-166 (1997).
[23] R. J. Trew, Proc. IEEE **90** 1032 (2002).
[24] W. J. Choyke, H. Matsunami, and G. Pensl, Silicon Carbide—A Review of Fundamental Questions and Applications to Current device Technology, (Wiley-VCH, Berlin, 1997).
[25] Ioffe Physico-Technical Institute, http://www.ioffe.ru/SVA/NSM/Semicond/SiC.
[26] S. M. Sze, Physics of Semiconductor Devices, 2nd ed., (Wiley-Interscience, New York, 1981)
[27] T. P. Chow, N. Ramungul, J. Fedison, and Y. Tang, SiC Power Bipolar Transistors and Thyristors, Silicon Carbide: Recent Major Advances, Eds. W. J. Choyke, H. Matsunami, and G. Pensl, 737 (Springer, Berlin, 2003).
[28] G. Pensl, H. Morkoc, B. M. Monemar and E. M. Janzen, Silicon Carbide, III-Nitrides, and Related Materials, (Trans Tech Publications, Switzerland, 1998).

[29] A. L. Spetz and S. Savage, Advances in SiC Field Effect Gas Sensors, Silicon Carbide: Recent Major Advances, Eds. W. J. Choyke, H. Matsunami, and G. Pensl, 869 (Springer, Berlin, 2003).
[30] R. T. Kemerley, H. B. Wallace, and M. N. Yoder, Impact of wide Bandgap Microwave Devices on DoD Systems, Proc. IEEE **90** 1059 (2002).
[31] S. J. Pearton, J. C. Zolper, R. J. Shul, and F. Ren, J. Appl. Phys. **86** 1 (1999).
[32] A. Lloyd Spetz, A. Baranzahi, P. Tobia, and I. Lundström, Phys. Stat. Sol. (a) **162** pp. 493-511 (1997).
[33] P. G. Neudeck, Steven L. Garverick, David J. Spry, Liang-Yu Chen, Glenn M. Beheim, Michael J. Krasowski, and Mehran Mehregany, Phys. Stat. Sol. (a), **206** pp. 2329-2345 (2009).
[34] G. W. Hunter, P. G. Neudeck, J. Xu, D. Lukco, A. Trunek, M. Artale, P. Lampard, D. Androjna, D. Maker, B. Ward, and C.C. Liu, MRS Proceedings, **815** (2004).
[35] Robert P. Devaty, Michael Dudley, T. Paul Chow and Philip G. Neudeck, Mater. Sci. Forum **717-720** pp. 1215-1218 (2004).
[36] Cree Inc., http://www.cree.com.
[37] J. Edmond, H. Kong, A. Suvorov, D. Waltz, and C. Carter, Jr., Phys. Stat. Sol., A **162** 481 (1997).
[38] J. Edmond, A. Abare, M. Bergman, J. Bharathan, K. Lee Bunker, D. Emerson, K. Haberern, J. Ibbetson, M. Leung, P. Russel, and D. Slater, J. Cryst. Growth **272** 242 (2004).
[39] H. Schulz and K. H. Thiemann, Solid State Commun. **23** 815 (1977).
[40] E. Gabe, Y. LePage, and S. L. Mair, Phys. Rev. B **24** 5634 (1981).
[41] V. A. Fomichev, Fiz. Tverd. Tela (Leningrad) **10** 763 (1968) [Sov. Phys. Solid State **10** 597 (1968)].
[42] G. A. Slack, J. Phys. Chem. Solids **34** 321 (1973).
[43] J. Duchene, Thin Solid Films **8** 69 (1971).
[44] W. M. Yim, E. J. Stofko, P. J. Zanzucchi, J. I. Pankove, M. Ettenberg, and S. L. Gilbert, J. Appl. Phys. **44** 292 (1973).
[45] I. Akasaki and H. Hashimoto, Solid State Commun. **5** 851 (1967)
[46] E. A. Irene, V. J. Silvestri, and G. R. Woolhous, J. Electron. Mater. **4** 409 (1975).
[47] J. Buer, L. Biste, and D. Bolze, Phys. Stat. Sol. (a) **39** 173 (1977).
[48] W. M. Yim and R. J. Paff, J. Appl. Phys. **45** 1456 (1974).
[49] P. B. Perry and R. F. Rutz, Appl. Phys. Lett. **33** 319 (1978).
[50] T. L. Tansley, E. M. Goldys, M. Godlewski, B. Zhou and H. Y. Zuo, in "GaN and Related Materials", Ed. by S. J. Pearton, p. 233 (Gordon and Breach, 1997).
[51] S. Yoshida, S. Misawa, and S. Gonda, J. Vac. Sci. Technol. B, **1** pp. 250-253 (1983).
[52] N. Sarazin, E. Morvan, M. A. di Forte Poisson, M. Oualli, C. Gaquiere, O. Jardel, O. Drisse, M. Tordjman, M. Magis, S-L Delage, IEEE Electron Device Lett., **31** pp.11-13 (2010).
[53] J. Kuzmik, IEEE Electron Device Lett., **22** pp.510-512 (2001).
[54] J. Xie, X. Ni, M. Wu, J. H. Leach, and H. Morko, Appl. Phys. Lett., **91** pp.132116 (2007)
[55] K. Davitt, Y.-K. Song, W. Patterson, A. V. Nurmikko, Z. Ren, Q. Sun, and J. Han, Phys. Stat. Sol. (a) **204** 2112 (2007)
[56] Toshio Nishida, Toshiki Makimoto, Hisao Saito and Tomoyuki Ban, Appl. Phys. Lett. **84**, 1002 (2004)
[57] Kentaro Nagomatsu, Narihito Okada, Hiroki Sugimura, Hirotoshi Tsuzuki, Fumiaki Mori, Kazuyoshi Iida, Akira Bando, Motoaki Iwaya, Satoshi Kamiyama, Hiroshi Amano, Isamu Akasaki, J. Crystl. Growth, **310** pp. 2326-2329 (2008).
[58] Chrstie Chatterley and Karl Linden, J. Water Health, **8** pp. 479-486 (2010).
[59] Jinhan Mo, Yinping Zhang, Qiujian Xu, Jennifer Joaquin Lamson, Rongyi Zhao, Atmos. Environ., **43** pp. 2229-2246 (2009).
[60] Asif Khan, K. Balakrishnan and T. Katona, Nat. Photonics, **2** pp. 77-84 (2008).

[61] S. Vilhunen, H. Sarkka, and M. Sillanpaa, Environ. Sci. Pollut. Res. **16** 439 (2009).
[62] J. A. Lely, Ber. Dt. Keram. Ges., **32** 299 (1955).
[63] Y. M. Tariov and V. F. Tsvetkov, J. Cryst. Growth **43** 209 (1978).
[64] Y. M. Tairov, and V. F. Tsvetkov, J. Cryst. Growth **52** 146 (1981).
[65] Kullaiah Byrappa, Tadashi Ohachi, "Crystal Growth Technology", pp. 189-191 (William Andrew, New York, 2013).
[66] G. Ziegler, P. Lanig, Dietmar Theis, C. Weyrich, IEEE Transactions on Electron Devices, **30**, pp. 277-281 (1983).
[67] Noboru Ohtani, Tatsuo Fujimoto, Masakazu Katsuno, Takashi Aigo, Hirokatsu Yashiro, J. Crystl. Growth, **237-239** pp. 1190-1186 (2002).
[68] T. S. Sudarshan, S. I. Maximenko, Microelectron. Eng., **83** pp. 155-159 (2006).
[69] II-VI Incorporated, http://www.iiviwbg.com/products.html.
[70] Dow Corning, http://www.dowcorning.com.
[71] G. A. Slack, T. F. McNelly, J. Cryst. Growth **34** 263 (1976).
[72] G. A. Slack, T. F. McNelly, J. Cryst. Growth **42** 560 (1977).
[73] Cengiz M. Balkas, Zlatko Sitar, Tsvetanka Zheleva, L. Bergman, R. Nemanich, R. F. Davis, J. Crystl. Growth, **179** pp. 363-370 (1997).
[74] Robert T. Bondokov, Stephan G. Mueller, Kenneth E. Morgan, Glen A. Slack, Sandra Schujman, Mark C. Wood, Joseph A. Smart, Leo J. Schowalter, J. Cryst. Growth, **310** pp. 4020-4026 (2008).
[75] R. Dalmau, Z. Sitar, "Sublimation Growth of AlN Crystals", Editors-in-Chief: K. H. Jürgen Buschow, Robert W. Cahn, Merton C. Flemings, Bernard Ilschner (print), Edward J. Kramer, Subhash Mahajan, and Patrick Veyssière (updates), In: Encyclopedia of Materials: Science and Technology 2nd Edition, pp. 1-9 (Elsevier, Oxford, 2005).
[76] R. Radhakrishnan Sumathi, Cryst. Eng. Comm. **15** pp. 2232-2240 (2013).
[77] J. H. Edgar, L. Liu, B. Liu, D. Zhuang, J. Chaudhuri, M. Kuball, S. Rajasingam, J. Cryst. Growth, **246** pp. 187-193 (2002).
[78] N. B. Singh, A. Berghman, H. Zhang, Tracy Wait, R. Chris Clarke, J. Zingaro, J. C. Golombeck, J. Cryst. Growth, **250** pp. 107-112 (2003).
[79] P. Lu, R. Collazo, R. F. Dalmau, G. Durkaya, N. Dietz, B. Raghothamachar, M. Dudley, Z. Sitar, J. Cryst. Growth, **312** pp. 58-63 (2009).
[80] Woo Sik Yoo and Hiroyuki Matsunami, Jpn. J. Appl. Phys., **30** 545 (1991).
[81] B. Raghothamachar, G. Dhanaraj, J. Bai, and M. Dudley, Microsc. Res. Tech. **69** pp. 343-358 (2006).
[82] St.G. Müller, in S*uperlattices and Microstructures*, **40** pp. 195-200 (Spring Meeting of the European Materials Research Society, Nice, France, 2006).
[83] P. G. Neudeck, Mater. Sci. Forum, **338-342** 1161 (2000).
[84] Q. Wahab, A. Ellison, A. Henry, E. Janzen, C. Hallin, J. Di Persio, and R. Martinez, Appl. Phys. Lett. **76** 2725 (2000).
[85] R. Singh, Microelectron Reliab., **46** 713 (2006).
[86] P. Bergman, H. Lendenmann, P. A. Nilsson, U. Lindefelt, and P. Skytt, Mater. Sci. Forum, **353-356** 299 (2001).
[87] R. E. Stahlbush, M. Fatemi, J. B. Fedison, S. D. Arthur, L. B. Rowland, and S. Wang, J. Electron. Mater. **31** 370 (2002).
[88] R.E. Stahlbush, K. X. Liu, and M. E. Twigg, in *IRPS Conf. Rec.*, **26-30** pp.90-94 (IEEE, San Jose, 2006).
[89] V.D. Wheeler, B.L. VanMil, R.L. Myers-Ward, C.R. Eddy, R.E. Stahlbush, and D.K. Gaskill, pp.1-2, 9-11 (ISDRS, Stamp College Park, MD, 2009).

[90] X. Zhang, M. Skowronski, K. X. Liu, R. E. Stahlbush, J. J. Sumakeris, M. J. Paisley, and M. J. O'Loughlin, J. Appl. Phys. **102** 093520 (2007).
[91] V. W. Berg, Naturwiseenschaften, **19** pp. 391-396 (1931).
[92] C. S. Barrett, Trans. Am. Inst. Min. Eng., **161** pp. 15-65 (1945).
[93] W. Wooster and W. A. Wooster, Nature, **155** 786 (1945).
[94] W. L. Bond and J. Andrus, Am Mineral, **37** pp. 622-632 (1952).
[95] L. G. Schulz, J. Met. **6** pp. 1082-1083 (1954).
[96] A. R. Lang, J. Appl. Phys., **29** 597 (1958).
[97] T. Tuomi, K. Naukkarinen, and P. Rabe, Phys. Status Solidi A, **25** pp. 93-106 (1974).
[98] Michael Hart, J. Appl. Cryst., **8** 436 (1975).
[99] W. M. Vetter and M.Dudley, J. Appl.Cryst. **35** 689 (2002).
[100] W. M. Zachariasen, in: Theory of X-ray Diffraction in Crystals, (Dover Publcations, Inc. Mineola, N. Y. 1945)
[101] B. W. Batterman and H. Cole, Rev. Mod. Phys., **36** pp. 681-717 (1964).
[102] A. Authier, Adv. X-ray Anal., **10** pp. 9-31 (1967).
[103] M. Katsuno, N. Ohtani, J. Takahashi, H. Yashiro, M. Kanaya, Jpn. J. Appl. Phys. **38** 4661 (1999).
[104] W. Chen and M. A. Capano, J. Appl. Phys., **98** 114707 (2005).
[105] H. Z. Song and T. S. Sudarshan, Mater. Sci. Forum, **125** pp. 717-720 (2012).
[106] R. T. Bondokov, I. I. Khlebnikov, T. Lashkov, E. Tupitsyn, G. Stratiy, Y. Khlebnikov and T. S. Sudarshan, Jpn. J. Appl. Phys., **41** 7312 (2002).
[107] B. Kallinger, S. Polster, P. Berwian, J. Friedrich, G. Müller, A.N. Danilewsky, A. Wehrhahn, A.D. Weber, J. Cryst. Growth, **314** pp. 21-29 (2011).
[108] H. Tsuchida, I. Kamata, M. Nagano, J. Cryst Growth **306** pp. 254-261 (2007).
[109] S.A. Sakwe, R. Müller, P.J., J. Cryst. Growth, **289** pp. 520-526 (2006).
[110] Y. Ishikawa, Y. Yao, Y. Sugawar, K. Danno, H. Suzuki, Y. Kawai and N. Shibata, Mater. Sci. Forum, **717-720** 367 (2012).
[111] Yi Chen, *Defects Structures in Silicon Carbide Bulk Crystals, Epilayers and Devices,* Ph.D. Thesis. Stony Brook University, U.S. (2009) (http://hdl.handle.net/1951/45064)
[112] Hexa Tech Inc. http://www.hexatechinc.com/